

**UCSF**

**UC San Francisco Electronic Theses and Dissertations**

**Title**

Mechanisms of cellular coordination in the assembly and function of tissues in Hydra

**Permalink**

<https://escholarship.org/uc/item/9sx5k33f>

**Author**

Skokan, Taylor Daniel

**Publication Date**

2022

Peer reviewed|Thesis/dissertation

Mechanisms of cellular coordination in the assembly and function of tissues in Hydra

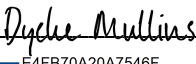
by  
Taylor Daniel Skokan

DISSERTATION  
Submitted in partial satisfaction of the requirements for degree of  
DOCTOR OF PHILOSOPHY

in  
Biochemistry and Molecular Biology

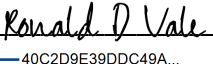
in the  
GRADUATE DIVISION  
of the  
UNIVERSITY OF CALIFORNIA, SAN FRANCISCO

Approved:

DocuSigned by:  
  
E4FB70A20A7546F... Dyche Mullins  
Chair

DocuSigned by:  
  
494DC... Sophie Dumont

DocuSigned by:  
  
494DC... Manu Prakash

DocuSigned by:  
  
494DC... Ronald D Vale

---

Committee Members

Copyright 2022

by

Taylor Daniel Skokan

## ACKNOWLEDGEMENTS

This work would not have been possible without the support of my graduate advisor, Ron Vale. When I came to the lab with the audacious (and naïve) desire to step outside the traditional bounds of the Vale Lab, Ron embraced this possibility wholeheartedly and delivered the two most important ingredients for any curiosity-driven scientist: immense freedom to explore, as illustrated by the disparate projects described in this dissertation, and a remarkable environment to support these pursuits. The latter is best illustrated by the incredibly talented individuals with whom I have had the pleasure of working over the past several years. I have been trained, challenged, humbled, inspired, encouraged, consoled, entertained, and enabled (for better or worse) by the many members of the Vale lab who have come and gone during this time. To those individuals—you know who you are—I have learned so much from each and every one of you, and I thank you.

Among this group, one individual warrants a special thanks: Kara McKinley. No single word exists to describe the gratitude I owe to Kara for her mentorship, yet any attempt to expound upon my indebtedness is doomed to read as hyperbole. Working with Kara has been nothing short of a masterclass in experimentation, communication, professionalism, mentorship, and advocacy. Despite Kara's ever-present guidance, thanks to her selfless execution—never seeking praise, credit, or even attention for these efforts—few will ever know the tireless hours of discussion, countless manuscript revisions, and agonizing consideration that Kara has invested in my success, or the extent to which her mentorship has shaped the scientist I am today.

I am additionally thankful for the many individuals who provided an extended professional support network during my time at UCSF. In particular, thank you to the members of my thesis committee: Dyche Mullins, Sophie Dumont, and Manu Prakash. Rarely have I enjoyed discussions

more than the committee meetings I shared with these brilliant minds. Even at my lowest points, their curiosity, creativity, and wisdom never failed to delight, stimulate, and inspire. Thanks also to our friends and colleagues in the *Hydra* research community, especially Celina Juliano, Rob Steele, and Bert Hobmayer, for welcoming us into their community with open arms; without their generosity and insights, this work would not exist. I am also deeply grateful to Ophir Klein for his seemingly boundless generosity in providing professional guidance and technical support throughout my training. Finally, thank you to my classmates; members of the Dumont, Prakash, Juliano, and Klein Labs; and the many colleagues at UCSF and beyond who brought encouragement, joy, and meaning to this long and difficult endeavor.

I would be remiss to ignore the remarkable mentors who fostered in me the passion for exploration and learning that made any of this a possibility. To Micha Miller and the extraordinary faculty and staff at Columbia College, who recognized and kindled the curiosity of a wandering and wayward community college student, thank you. To Jessica Feldman, who first put a pipette in my hand and whose outrageously infectious creativity, enthusiasm, and brilliance stoked that curiosity to a blazing inferno, thank you.

Thank you to my family for their undying love, patience, and support, past and present; you have all made me the person I am today. Thank you, especially, to my mother and brothers—Louise, Andrew, and Matt—and Kim, Peg, Melissa, and the rest of the Fong family. Lucky is having one amazing family to lean on and learn from; charmed is having two, as I most fortunately do. Thank you to Lily Tomlin, for the limitless love, faith, and joy you have shown me. And, with the deepest love and humility, thank you to my partner, Alex. For bearing with, building up, talking down, tuning out, or whatever I was in need of at the time, I am forever thankful for you and your love, patience, and support throughout these years.

Though lonely at times, earning a PhD is no solo endeavor. While this work bears my name, this dissertation reflects the hours, efforts, aspirations, and ideas of all those who have supported and inspired me to and through this stage of my life. A fair and comprehensive list of these names and contributions would amount to far more than the pages allotted for this document. Thus, my sincere thanks extend well beyond the names highlighted above.

Lastly, this dissertation also reflects a profound degree of privilege—not only the privilege that brought me to graduate school, but the privilege to choose this path, toiling away at problems for which there exists no immediate demand for solutions, my basic needs and security largely accounted for. While this statement cannot, and should not, diminish the hard work and noble effort involved in knowledge production, may it serve as a lingering reminder to myself and others of the biases inherent in our systems of knowledge production.

## CONTRIBUTIONS

Chapter 2 of this dissertation contains partial reprints of the following previously published material:

Skokan, T.S., Vale, R.D., McKinley, K.L. (2020) Cell sorting in *Hydra vulgaris* arises from differing capacities for epithelialization between cell types. *Current Biology*. 30(19), 3713–3723.

Chapter 3 of this dissertation contains ongoing work and partial reprints of the following previously preprinted material:

Skokan, T.S., Hobmayer, B., McKinley, K.L., Vale, R.D. (2021) Mechanical stretch regulates macropinocytosis in *Hydra vulgaris*. *BioRxiv*. doi:10.1101/2021.12.03.471193.

## ABSTRACT

### **Mechanisms of cellular coordination in the assembly and function of tissues in *Hydra***

Taylor Daniel Skokan

The proper organization and coordination of cells is essential to the integrity and function of tissues, organs, and multicellular organisms. While diverse organs and organisms have been used to study these foundational principles, the sheer structural and compositional complexity of many *in vivo* experimental models raises numerous challenges to dissecting the cellular mechanisms underlying their formation and function. Conversely, *in vitro* models, despite limiting structural complexity, frequently fail to recapitulate the complete physiology of the organs from which they are derived. To ameliorate these tradeoffs, we exploited the anatomical simplicity and extraordinary regenerative capacity of the basal metazoan *Hydra vulgaris* to probe the mechanisms of tissue patterning and coordinated cellular physiology. In Chapter 2, we apply live microscopy and physical cellular manipulation to investigate a decades-old observation in which a disordered aggregate of *Hydra* cells sorts into inner and outer epithelial compartments, a prerequisite to regenerating a functional body plan. We show that differences in the rates of epithelialization between two primary cell types give rise to the bilayered structure of the intact animal. In Chapter 3, we investigate the function of these assembled tissues. Specifically, through the identification and dissection of a fluid engulfment phenomenon known as macropinocytosis, we reveal a role for tissue mechanics in regulating fluid uptake and membrane recycling in homeostatic *Hydra* epithelia. Together, these studies illustrate how the emergent properties of cell collectives, such as cell polarity and tissue mechanics, can contribute to the structure and function of living animals.



## TABLE OF CONTENTS

<b>CHAPTER 1</b>	<b>1</b>
Introduction and Summary	1
<b>CHAPTER 2</b>	<b>6</b>
<b>Cell sorting in <i>Hydra vulgaris</i> arises from differing capacities for epithelialization between cell types</b>	<b>6</b>
Abstract	6
Introduction	7
Results	9
Discussion	16
Figures and figure legends	21
Supplemental figures/tables and legends	29
Materials and methods	35
Acknowledgments	40
<b>CHAPTER 3</b>	<b>41</b>
<b>Mechanical stretch regulates macropinocytosis in <i>Hydra vulgaris</i></b>	<b>41</b>
Abstract	41
Introduction	41
Results	43
Discussion	47
Figures and figure legends	52
Supplemental figures/tables and legends	58
Materials and methods	62
Acknowledgments	65
<b>CHAPTER 4</b>	<b>67</b>
Final Thoughts	67
<b>REFERENCES</b>	<b>71</b>

## LIST OF FIGURES

### CHAPTER 2

Figure 2.1	21
Figure 2.2	23
Figure 2.4	27
Figure 2.5	28
Figure S2.1	29
Figure S2.2	31
Figure S2.3	33
Figure S2.4	34

### CHAPTER 3

Figure 3.1	52
Figure 3.2	54
Figure 3.3	56
Figure 3.4	57
Figure S3.1	58
Figure S3.2	59
Figure S3.3	61

# CHAPTER 1

## Introduction and Summary

Tissues and organs require the proper positioning and coordinated efforts of vast networks of cells to properly function. Cellular coordination can be achieved in many ways and, similarly, support diverse processes essential to development and homeostasis. For instance, the cells of a tissue may be mechanically linked to neighbors via cell junctions or supracellular actin networks, enabling the formation of barriers to the outside environment (reviewed in [1]) and allowing cells to withstand and exert the forces required to shape tissues and close wounds (reviewed in [2]). Cells may further be chemically linked through local diffusion networks, gap junctions, or, for even greater reach, neural circuits, facilitating the rapid relay of information across large length scales (reviewed in [1,3]). Ultimately, this cooperativity enables the emergence of functional domains, which execute the many requirements of anatomical structures, from mechanical support and compartmentalization to signaling and self-renewal.

One extraordinary manifestation of cell coordination is cellular self-organization, a process by which global patterns emerge through the cumulative effects of local interactions between cells. The first insights into self-organization arose from classic experimental embryology and regenerative biology, which revealed that specific cell populations (“organizers”), when repositioned within embryos or mature animals, could induce changes in the development and regeneration of the animal form [4–6]. Remarkably, these principles were later shown to apply even in instances in which developmental processes and anatomical structures were severely disrupted; in particular, it was shown that embryonic tissue explants, when recombined, were capable of reorganizing to partially restore the native organization of the intact embryo, in some

cases through the segregation, or “sorting,” of cells by tissue of origin [7]. These pioneering discoveries underscored the potential for self-organization amongst cells and brought the principles of self-organization to the forefront of developmental and regenerative biology.

How discrete cells coordinate local interactions to establish large and complex structures, like the embryo, has remained a central topic of exploration since those initial discoveries. With the dawn of the molecular biology era came the ability to dissect the cellular factors contributing to emergent tissue patterns. Early experiments focused on local adhesive forces, based on observed parallels between biological systems and physical sorting phenomena [7,8] and subsequent experiments revealing that cell sorting could be predicted by the strength of adhesions within the contributing tissues [9]. This notion was further validated by the observation that changes in the identity and expression levels of cell adhesion molecules, known as cadherins, were sufficient to drive the spontaneous segregation of otherwise identical cell populations in tissue culture [10–12]. This work lent credence to the profoundly influential “differential adhesion hypothesis” (DAH), which credited cell affinities, based on adhesion and tissue surface tension, as drivers of cell sorting [13]. The DAH and, later, the related differential interfacial tension hypothesis (DITH) [14,15] provided useful biophysical lenses with which to analyze the principles of cellular self-organization. These perspectives shaped much of the experimental landscape for decades, giving rise to a sizable body of literature supporting roles for adhesion and interfacial tension in self-organization both *in vitro* and *in vivo* (reviewed in [16]).

Despite undeniable roles for tissue surface tension and cellular affinity in cell sorting, technical limitations have made definitively testing their contributions in physiological settings, in contrast to the highly controlled *in vitro* and *in silico* models used to first inform these hypotheses, difficult. Moreover, observing and dissecting the cellular processes and properties underlying these

biophysical properties in complex living tissues, where they may be obfuscated or inextricably interwoven, raises additional challenges. Nevertheless, in several instances, rigorous comparisons of the mechanisms driving sorting in biologically related *in vitro* and *in vivo* experimental systems have been possible, revealing discordances that point to limitations of the DAH and DITH in physiological contexts [17–19]. Together, these realizations suggest a requisite compromise between *in vivo* studies of conventional model organisms and simplified *in vitro* experimental models.

An ideal system to study self-organization and cell coordination would simultaneously minimize complexity and capture the complete physiology of the tissue in question. While recent years have seen tremendous advances, and increasing fidelity, in *in vitro* tissue culture models (reviewed in [20,21]), an alternative tack is to look to nature for simple and accessible animal models. In this vein, the freshwater cnidarian *Hydra vulgaris* is a particularly attractive candidate, due to its relatively simple body plan and remarkable regenerative capacity. *Hydra* is a radially symmetric animal with a body axis defined by an adherent foot (“peduncle”) and opposing mouth (“hypostome”) and tentacles. Microscopically, the entire body plan consists of two, concentric epithelial monolayers—an outer “ectoderm” and inner “endoderm”—separated by an extracellular matrix (“mesoglea”) and interspersed with neurons and other specialized cell types [22]. This simple anatomy, combined with the animal’s transparency, renders *Hydra* similarly accessible, both physically and optically, to many minimal tissue culture models. Recently devised methods for generating transgenic animals [23] have further contributed to its tractability as a model of self-organization, animal physiology, and cell biology.

Recent studies of cell and tissue coordination in *Hydra* build on a longstanding fascination with *Hydra* biology and regeneration that dates back to the 18<sup>th</sup> century [24]. Beyond the ability to

achieve full-body regeneration from a small fragment of intact tissue [24], *Hydra* is also capable of rapidly reassembling a functional body plan from dissociated and reaggreated cells, a feat that requires first sorting endodermal and ectodermal epithelial cells into their respective inner and outer compartments [25]. This ability to restore full functionality to a completely disordered aggregate of cells makes *Hydra* a uniquely powerful model of self-organization.

As with previous cell sorting models, the DAH and DITH have been invoked to explain the re-compartmentalization of cell types in *Hydra* following reaggregation [25,26]. Indeed, measurements of tissue surface tension have revealed differences between endodermal and ectodermal tissues [26,27], and *in silico* modeling suggests that these differences are sufficient to drive spontaneous tissue segregation [27]. However, the lack of molecular tools required to precisely modulate cadherin expression or tissue surface tension have made direct challenges to this model difficult. Furthermore, quantification of the adhesive strength of isolated ectodermal and endodermal cells suggests that heterotypic interactions between these cell types are unfavorable, conflicting with the predictions of the DAH with respect to the sorting outcomes observed in *Hydra* [28]. While direct observation of cell behaviors in *Hydra* reaggreats has been leveraged in an attempt to resolve these disagreements, these studies largely predated the availability of transgenic reporters or were otherwise limiting in their imaging resolution [27,29–32]. Thus, in Chapter 2, we revisit the role of cell behaviors in the sorting of *Hydra* reaggreats, combining transgenic approaches with modern microscopy and physical manipulation to reveal how emergent multicellular properties determine the positioning of cell lineages. This work highlights the importance of foundational cellular features, like cell polarity, often overlooked by simple biophysical models of cell sorting.

Importantly, emergent multicellular properties play essential roles in other aspects of *Hydra* biology, extending well beyond the requirement for sorting. For instance, *Hydra* epithelial cells exhibit extensive connections via gap junctions, allowing for the rapid conduction and synchronization of signals across the body tissues [33–35]. *Hydra* epithelia also exhibit an organismal-scale planar cell polarity. While this polarity likely plays a role in orienting cell divisions in the epithelia [36], it is arguably best illustrated by contractile structures called myonemes, which align in stereotypical patterns throughout the animal and perform the contractile functions necessary for locomotion [37]. Thus, *Hydra* depends on the organization and coordination of cells for numerous homeostatic physiological processes, making it a powerful and accessible model for studying coordinated cell biology. In Chapter 3, we explore this notion further, detailing the serendipitous discovery of a tissue-scale form of macropinocytosis in *Hydra*, and the effects of mechanical tension on this process.

By combining classic and modern approaches to the study of an anatomically simple animal, our work sheds light on the role of cellular context in shaping cell behaviors during regeneration and homeostasis in *Hydra*. Though disparate in nature, when taken together, these works highlight the value of under-explored experimental models for both gaining new insights into classic problems and uncovering unexpected biology.

## CHAPTER 2

### Cell sorting in *Hydra vulgaris* arises from differing capacities for epithelialization between cell types

#### Abstract

*Hydra vulgaris* exhibits a remarkable capacity to reassemble its body plan from a disordered aggregate of cells. Reassembly begins by sorting two epithelial cell types, endoderm and ectoderm, into inner and outer layers, respectively. The cellular features and behaviors that distinguish ectodermal and endodermal lineages to drive sorting have not been fully elucidated. To dissect this process, we use micromanipulation to position single cells of diverse lineages on the surface of defined multicellular aggregates and monitor sorting outcomes by live imaging. Although sorting has previously been attributed to intrinsic differences between the epithelial lineages, we find that single cells of all lineages sort to the interior of ectodermal aggregates, including single ectodermal cells. This reveals that cells of the same lineage can adopt opposing positions when sorting as individuals or a collective. Ectodermal cell collectives adopt their position at the aggregate exterior by rapidly reforming an epithelium that engulfs cells adhered to its surface through a collective spreading behavior. In contrast, aggregated endodermal cells persistently lose epithelial features. These non-epithelialized aggregates, like isolated cells of all lineages, are adherent passengers for engulfment by the ectodermal epithelium. We find that collective spreading of the ectoderm and persistent de-epithelialization in the endoderm also arise during local wounding in *Hydra*, suggesting that *Hydra*'s wound-healing and self-organization capabilities may employ similar mechanisms. Together, our data suggest that differing propensities for epithelialization can sort cell types into distinct compartments to build and restore complex tissue architecture.



## Introduction

Defining the mechanisms that organize cells into distinct compartments in the body is critical for understanding development and regeneration, and has facilitated the development of synthetic models of complex biological tissues and structures [20]. Pioneering work by Townes and Holtfreter showed that dissociated cells from the amphibian embryo spontaneously sort from one another when recombined, reforming distinct layers reminiscent of their native organization [7]. Mechanistic dissection of this sorting phenomenon can provide fundamental insights into how cellular properties give rise to tissue organization across diverse systems.

Previous studies in a variety of experimental models point to cell-intrinsic differences as crucial drivers of cell sorting (reviewed in [38]). In particular, differences in adhesion strength or biophysical properties between cell types can affect sorting outcomes, lending support to models like the differential adhesion hypothesis (DAH) and differential interfacial tension hypothesis (DITH) [8,11,15,19,39,40]. These models broadly attribute sorting to differences among cell types that affect the areas of cell contacts until energetically favorable configurations are achieved (Brodland, 2002; Steinberg, 1962a, 1962b). In addition to the contributions of cell-intrinsic differences, cell positioning can also be affected by features of a cell's surroundings. For example, neighboring cells locally modulate cell behaviors and properties at compartment boundaries in the *Drosophila* wing disc and *Xenopus* embryo [41–43]. How cell-intrinsic and -extrinsic factors intersect to govern cell position remains unclear.

The freshwater cnidarian *Hydra vulgaris* is a particularly powerful model of cellular self-organization, as *Hydra* can reassemble its entire body plan from a collection of dissociated cells within days [25]. The *Hydra* body plan is largely defined by two epithelial compartments—an inner layer termed the endoderm and an outer layer termed the ectoderm—organized as concentric

monolayers separated by an extracellular matrix (**Fig. 2.1A**). A third, interstitial cell lineage includes neurons, gland cells, and specialized stinging cells (nematocytes) scattered throughout the body [22]. Following dissociation and reaggregation, the endodermal and ectodermal compartments are rapidly reestablished as the first major step toward rebuilding the animal [25,26,44]. Cell proliferation and trans-differentiation are minimal or absent during these early stages, underscoring the central role for cell sorting in rebuilding the *Hydra* body plan [25,26]. *Hydra* represents a unique model in which rapid cell sorting gives rise to functional tissues.

In *Hydra*, cell-intrinsic differences in biophysical properties and motility have been proposed as key drivers of endodermal/ectodermal cell sorting. Specifically, endodermal and ectodermal lineages exhibit different interfacial tensions and adhesive properties largely consistent with the requirements of the DAH and DITH described above [26–28,45]. Differences in endodermal and ectodermal cell motility have also been proposed to drive sorting [29,30]. However, attempts to track large numbers of cells during this process failed to show lineage-specific differences in the speed or directionality of migration [27,31,32]. Thus, despite evidence for biophysical properties contributing to sorting, previous approaches have left many unanswered questions regarding the cellular interactions underlying rapid compartmentalization in *Hydra*.

Here, we combine cellular micromanipulation and live microscopy to dissect the mechanisms of cell sorting in *Hydra*. Surprisingly, we find that single cells of all lineages, including ectodermal cells, sort to the interior of ectodermal aggregates. We find that aggregated ectodermal cells rapidly reform a polarized epithelial monolayer, which indiscriminately engulfs cells adhered to its surface by a wound healing-like process. Cells that are unable to rapidly reform an epithelium, such as endodermal aggregates and isolated ectodermal cells, readily adhere to the ectodermal epithelium and are positioned at the aggregate interior during engulfment. Together,

our data suggest that a key feature distinguishing the ectoderm and endoderm and driving their sorting is their capacity for rapid multicellular organization. We find that differences in the maintenance and restoration of epithelial organization between the ectoderm and endoderm arise during both self-organization and local wound healing, suggesting that common mechanisms may underlie regeneration at cellular and organismal scales. Overall, our data support a model in which cell sorting can be driven by differences in re-epithelialization among distinct cell populations.

## Results

### **Ectodermal aggregates internalize diverse Hydra cell types, including isolated ectodermal cells**

The predominant models for cell sorting in *Hydra* propose that intrinsic differences in the properties of endodermal and ectodermal cells direct them to sort into interior and exterior compartments, respectively. We sought to directly test this role for cell identity in directing sorting, as well as to identify cellular behaviors that may not be reflected in existing models. To this end, we first developed a method that rendered the sorting process amenable to physical manipulation and high-resolution microscopy. Historically, sorting in *Hydra* has been analyzed by combining dissociated cells by centrifugation, which generates aggregates approximately 300-800  $\mu\text{m}$  in diameter or larger [25–27,44,46]. These aggregate preparation methods preclude study of the initial minutes of sorting, restrict physical control over the process, and generate limited cellular and subcellular resolution due to light scattering. Therefore, we developed an approach that allowed us to isolate aggregates of relatively small sizes to facilitate high-resolution imaging (approximately 60  $\mu\text{m}$ ; **Fig. S2.1A**, Methods). We combined this method with a microscope-

mounted micropipette aspirator to allow us to initiate interactions between specific lineages at precisely defined positions (**Fig. 2.1B**).

As a proof of principle, we first tested how ectodermal aggregates expressing a lineage-specific DsRed2 interacted with single GFP-expressing endodermal cells. As expected, isolated endodermal cells placed in contact with the surface of ectodermal aggregates were rapidly internalized and subsequently remained at the aggregate interior (**Fig. 2.1C, S2.1B**). In contrast, ectodermal cells placed in contact with endodermal aggregates were not internalized; instead, ectodermal cells adhered to and spread over the endoderm, as previously described for single cells and larger aggregates [29,30] (**Fig. 2.1D**). Thus, this micromanipulation approach facilitates controlled induction of cell sorting.

We employed our assay to directly test the role of cell identity in determining cell positioning by manually combining cells and aggregates of specific lineages (**Fig. 2.1B**). To this end, we placed DsRed2-expressing ectodermal aggregates in contact with GFP-expressing cells of all *Hydra* lineages, including interstitial stem cells, neurons, nematocytes, and ectodermal epithelial cells. We found that all cell types placed in contact with ectodermal aggregates were efficiently internalized and, like endodermal cells, remained within the aggregate for the duration of our experiments (**Fig. 2.1E, S2.1C, S2.1D**). Most surprisingly, ectodermal aggregates even internalized isolated ectodermal cells at high frequency (**Fig. 2.1E, 2.1F**). Thus, the ectoderm can robustly internalize a wide array of *Hydra* cell types, including cells of its own lineage, revealing that (1) cell sorting in *Hydra* does not depend on unique features of the endodermal lineage, and (2) the same lineage can experience opposing sorting outcomes when present as single cells as opposed to multicellular aggregates. Together, these findings demonstrate that cell lineage alone cannot be the determinant of whether cells adopt inner or outer positions during sorting.

## **Differences in epithelialization generate distinct adhesive properties between and within lineages**

As ectodermal aggregates internalized all cells independently of their identity, we sought to determine what distinguishes the ectodermal aggregate from the entities that it internalizes. During the development of the micromanipulation assay, we found that endodermal and ectodermal cells and aggregates exhibited striking differences in their capacity to establish stable contacts with other cells. The ectodermal aggregate was broadly unable to adhere to cells placed in contact with its surface (**Fig. 2.2A, 2.2B**). Instead, adhesion and subsequent internalization were restricted to morphologically distinct sites on the aggregate surface, which we term “hotspots” (**Fig. 2.2A, 2.2B, S2.2A**). These sites could be identified prior to manipulation by the presence of local membrane ruffling (**Fig. 2.2A**). Positioning cells in contact with these pre-identified sites was predictive of successful internalization (**Fig. 2.2B**). In contrast to the ectodermal aggregates, the entire surface of endodermal aggregates readily adhered when placed in contact with other cells (**Fig. 2.1D**). Importantly, both single endodermal cells and single ectodermal cells were also adherent (**Fig. 2.1C-2.1E**). Together, these findings reveal that all entities that are internalized exhibit uniform adhesion, whereas adhesion is spatially restricted in ectodermal aggregates.

The data described above demonstrated that ectodermal aggregates differ from both endodermal aggregates and, crucially, single ectodermal cells in their adhesive properties and the positions they adopt during sorting. To determine what gives rise to these differences, we compared aggregates and single cells of the ectodermal and endodermal lineages expressing LifeAct-GFP or myosin regulatory light chain-GFP (MRLC-GFP). Actomyosin localization functions as a reporter of tissue organization and polarity by labeling apical cell junctions in both the endoderm and ectoderm in intact *Hydra* [47,48], as in other epithelial tissues [49]. Although

LifeAct expression has been reported to affect actin in some systems [50,51], prior characterization in *Hydra* reported LifeAct localization consistent with endogenous actin organization at cell junctions, and no defects in major developmental or physiological processes [47]. Single cells of both epithelial lineages exhibited diffuse cortical actin localization (**Fig. 2.2C**), as expected for isolated cells in suspension [52]. Similar actin localization was observed in endodermal aggregates (**Fig. 2.2C**). Endodermal aggregates and isolated cells of both epithelial lineages also exhibited constitutive membrane blebbing (**Fig. S2.2B**), consistent with endodermal “pseudopods” previously suggested to drive sorting [30]. However, inhibiting endodermal blebbing with the myosin II inhibitor (S)-nitro-Blebbistatin had no discernible effect on internalization, suggesting that this behavior is nonessential for sorting (**Fig. S2.2C, S2.2D**). The disordered and dynamic nature of the endoderm and isolated ectodermal cells contrasted starkly with the architecture of ectodermal aggregates, which retained the characteristic junctional actomyosin organization observed in intact *Hydra* epithelia, with relatively smooth and stable aggregate surfaces (**Fig. 2.2C, S2.3A**). Thus, the epithelial entities that are internalized share common dynamics and actin architecture, despite their differing lineages.

Notably, the adhesion-permissive “hotspots” we identified on the surface of ectodermal aggregates were marked by local disorganization of the otherwise robust junctional actomyosin network (**Fig. 2.2D, S2.3A**). We found that hotspots arose either in response to local aggregate remodeling, for example at sites of spontaneous cell ingression (**Fig. 2.2D**), or where the edges of newly sheared ectodermal tissue fragments met to form spherical aggregates (**Fig. S2.3B**). These surface irregularities were frequently resolved over time as new cell-cell contacts were formed (**Fig. 2.2D, S2.3B**). Altogether, these findings suggest that hotspots reflect sites of local epithelial discontinuity. Thus, in contrast to their endodermal counterparts, ectodermal aggregates maintain

and restore epithelium-like architecture, which restricts cell adhesion to sites of epithelial discontinuity.

### **Restoration of ectodermal epithelial continuity positions cells in aggregate interiors**

We next sought to determine the cellular mechanisms by which ectodermal aggregates internalize cells following their adhesion to hotspots. To this end, we visualized ectodermal aggregates expressing LifeAct-GFP internalizing unlabeled endodermal aggregates. We observed a striking spreading and enveloping behavior of ectodermal cells surrounding captured endodermal aggregates. This process was characterized by the extension of dynamic, actin-rich protrusions from cells bordering sites of internalization. As the protrusive fronts of adjacent ectodermal cells met following internalization, new cell junctions formed to reestablish epithelial continuity (**Fig. 2.3A**). The protrusive and zippering behaviors were reminiscent of epithelial wound healing reported in other systems [53,54]. These data suggest that the ectodermal cell dynamics associated with restoring epithelial continuity drive the internalization of cells adhered to the aggregate surface.

Having identified these ectodermal cell behaviors associated with sorting in our small aggregate system, we next asked how these processes play out in large aggregates comparable to those used in previous sorting analyses ( $\geq 300\text{-}800\ \mu\text{m}$  diameter) [27,46]. We generated large aggregates containing both unlabeled endoderm and LifeAct-GFP-labeled ectoderm by centrifuging suspensions of dissociated cells, and used live microscopy to visualize cells in the most superficial layers of the resulting aggregates (**Fig. 2.3B**). Using this approach, we observed ectodermal cells spreading via actin-rich protrusions and gradually reintegrating into continuous epithelial patches. As with cell internalization (**Fig. 2.3A**), LifeAct-GFP accumulated at cell

junctions as new cell-cell contacts were established (**Fig. 2.3B**). These findings suggest that the ectodermal behaviors underlying cell sorting in small aggregates also restore ectodermal epithelial continuity on larger length scales.

### **Ectodermal epithelial architecture is rapidly reestablished following disruption**

Our observations above suggested that the conditions necessary for sorting arise as a consequence of the ectoderm's propensity to maintain and locally reestablish epithelial continuity. However, both large and small aggregates exhibited some degree of ectodermal epithelial architecture at the onset of these experiments. We, therefore, directly tested whether ectodermal cells can reestablish epithelial architecture de novo, starting from single cells. To this end, we used micromanipulation to manually reassemble ectodermal aggregates (~40-80  $\mu\text{m}$  diameter) from single cells expressing MRLC-GFP by iteratively adhering cells to one another (**Fig. 2.3C**). Despite their initial lobed appearance and diffuse myosin localization, manually assembled ectodermal aggregates gradually matured into roughly spherical structures, with myosin accumulating at newly formed cell junctions (**Fig. 2.3C, 2.3D**). Single endodermal cells also readily adhered to one another and could be manually reassembled into aggregates. However, we observed no indications of re-epithelialization in these aggregates (**Fig. 2.3D, S2.4**), consistent with the stable, but non-epithelialized, endodermal aggregates that arise from partial dissociation (**Fig. 2.2C**). These experiments confirm that the ectodermal lineage is not only predisposed to maintain and repair its epithelial architecture, but also to rapidly reestablish it following complete cellular dissociation.



### **Differential maintenance of epithelial architecture is recapitulated in local wounding**

In light of our observations that ectodermal continuity during sorting was restored through a wound healing-like process, we considered whether the lineage-specific epithelialization behaviors that we identified contributed to the response to other forms of epithelial disruption in the animal. To this end, we analyzed the cellular response of ectodermal and endodermal tissues to wounding. We excised living fragments from the *Hydra* body column and sequentially imaged these fragments near their center, to assess the properties of the intact monolayer, and at their edges, to monitor the properties of the wound front, where tissue continuity was locally disrupted (**Fig. 2.4A**). In the central regions, LifeAct-GFP localized to all cell-cell contacts in both the ectoderm and endoderm (**Fig. 2.4B, 2.4C**), as previously reported in the intact animal [47]. However, the epithelial lineages exhibited strikingly different behaviors at tissue boundaries. At the ectodermal wound front, LifeAct-GFP labeled both cell-cell contacts and a protrusive front at fragment edges (**Fig. 2.4B'**), analogous to the actin organization that we observed at sites of cell internalization in small aggregates (**Fig. 2.3A**). In contrast, at the endodermal wound front, LifeAct-GFP was no longer enriched at cell-cell contacts, but instead diffusely localized in wound-adjacent endodermal cells (**Fig. 2.4C'**). Additionally, endodermal cells at the wound front exhibited constitutive membrane blebbing (**Fig. 2.4C'**) analogous to that observed in endodermal small aggregates (**Fig. 2.2C, S2.2B**). Together, these findings reveal close parallels between cell sorting and wound healing in *Hydra*, and raise the possibility that lineage-specific differences in the maintenance and restoration of epithelial organization may factor more broadly into healing and regeneration in the animal.

## Discussion

*Hydra*'s ability to self-organize a viable organism from a disordered aggregate of cells provides a unique opportunity to study the mechanisms by which cells establish and maintain positioning to generate precisely patterned, functional tissues. Here, we recapitulated sorting in small aggregates to facilitate high-resolution live imaging and physical manipulation of the process. We found that, following dissociation and reaggregation, ectodermal cells rapidly reestablish epithelial architecture, in contrast to endodermal cells, which remain disordered. The epithelial architecture of the ectoderm restricts cell adhesion to sites of local discontinuity, where non-epithelialized cells are captured. Finally, ectodermal cell spreading restores epithelial continuity, thereby engulfing captured cells and positioning them to the aggregate interior. Based on these findings, we propose a model in which tissue-specific differences in epithelialization drive cell sorting (**Fig. 2.5**).

Previous investigations of cell sorting in *Hydra* have largely focused on distinguishing two competing models. One frequently evoked model proposes that ectodermal and endodermal cells sort based on their distinct biophysical properties [26,27]. In support of this model, previous work revealed a higher tissue surface tension in endodermal explants when compared to ectodermal explants, as predicted by common biophysical models of sorting like the differential adhesion hypothesis and the differential interfacial tension hypothesis [26,27]. An alternative model ascribes sorting to lineage-specific differences in the rate or direction of cell migration [29,30]. Broadly, both models emphasize cell-intrinsic differences between endodermal and ectodermal lineages that promote their partitioning to the interior and exterior of a cell aggregate, respectively. Our micromanipulation approach allowed us to directly test the role of cell identity in sorting. We found that ectodermal cells do not intrinsically adopt outer positions during sorting in all contexts, but can instead adopt inner or outer positions depending on whether they are presented as single

cells or multicellular aggregates (**Fig. 2.1C, 2.1E**). This discovery revealed that, to identify the determinants of sorting, the relevant comparison is not 1) ectodermal versus endodermal cells, but rather 2) ectodermal aggregates versus single cells of both lineages and endodermal aggregates.

Our data suggest that what distinguishes the ectodermal aggregate from internalized entities is the emergence of a polarized adhesive interface. All internalized entities, including single ectodermal cells and endodermal aggregates, are uniformly adhesive (**Fig. 2.1D, 2.1E, S2.1D**). In contrast, mature ectodermal aggregates fail to establish stable cell contacts with any cell type placed in contact with their intact apical interfaces (**Fig. 2.2A, 2.2B**). This is consistent with prior observations made in larger ectodermal explants, which resist fusion except at freshly cut interfaces [27]. These unique adhesive properties may arise as a result of the ectodermal aggregate's ability to rapidly reconstruct a polarized epithelial monolayer (**Fig. 2.3A-2.3C**). One mechanism by which this could occur is through the redistribution of adhesion molecules as polarity is established, as in ectodermal explants of *Xenopus* embryos, in which C-cadherin molecules redistribute exclusively to basolateral membranes and away from free apical interfaces following tissue condensation [55]. Due to the formation of a non-adherent ectodermal surface, cell adhesion is permitted exclusively where the ectodermal epithelium is transiently disrupted (hotspots), and adhered cells are subsequently internalized as these discontinuities are resolved (**Fig. 2.2A, 2.2B, 2.3A**). These results shed light on previous observations that *Hydra* aggregates transition from homotypic (comprised of a single epithelial cell type) to heterotypic (consisting of both ectodermal and endodermal cells) as aggregates expand in size in rotary culture [44]. We speculate that the increase in heterotypic interactions with size may result from an increase in hotspots as aggregate surface area increases.

Our findings support a relatively simple model through which a mixed aggregate can sort if one cell type is predisposed to generate and maintain a polarized monolayer. Under this model, hotspots, which we speculate arise from exposed membranes of the aggregate interior, are returned to the aggregate interior, along with any adhered entities, as ectodermal epithelial continuity and polarity are restored (**Fig. 2.5**). Intriguingly, this model, arising from our studies in adult *Hydra*, is consistent with frequently overlooked observations from Holtfreter's classic self-organization studies in the amphibian embryo. In particular, he reported that an epithelial sheet of superficial blastomeres (formerly known as the "surface coat") formed an apical barrier to adhesion that promoted its localization to the aggregate exterior in recombined explants [7,56,57]. Thus, selective epithelialization may play a role in determining cell positioning during sorting in diverse systems. Interestingly, while this mechanism can account for a bias toward lineage-specific cell sorting, the absence of explicit mechanisms to prevent the internalization of non-epithelialized ectodermal cells may also explain topological defects observed in prior studies of *Hydra* reaggregation, such as the presence of internalized ectodermal compartments that resolve over time [46]. We did not observe internalized cells, including ectodermal cells, reemerging to the aggregate surface in our experiments, suggesting that sorting error correction may occur over longer timescales or involve alternative mechanisms, such as cell death. Understanding the fate of internalized ectodermal cells and how topological defects within aggregates are resolved is an exciting direction for future study.

We found that the endoderm and ectoderm exhibit differing propensities to maintain and reestablish epithelial organization in a variety of contexts, including after disruption by wounding (**Fig. 2.4B, 2.4C**) or dissociation (**Fig. 2.2C, 2.3C, S2.4**). Importantly, we note that this selective epithelialization may not only restrict polarized adhesion to one lineage, as we describe here for

the ectoderm, but likely also influences interfacial tensions, and thus may impact sorting in multiple ways. The mechanisms that underlie these differing propensities for re-epithelialization remain unknown. We did not observe the restoration of epithelial architecture in endodermal aggregates following manual reassembly (**Fig. S2.4**) or partial dissociation (**Fig. 2.2C**), even when following these aggregates for several hours. While the small aggregates used in this study recapitulate the sorting behaviors seen in larger aggregates, small aggregates ultimately dissociate prior to luminogenesis, precluding more prolonged studies of endodermal re-epithelialization, as well as the study of later aspects of the *Hydra* regeneration process. For example, restoration of the extracellular matrix, which normally separates endodermal and ectodermal monolayers, is first observed almost a full day after reaggregation [58], which is beyond the lifetime of our small aggregates. Thus, it is intriguing to consider that endodermal epithelialization may depend on the restoration of the ECM or other features not present in the early stages of regeneration. Together, our data suggest that the capacity to polarize may be intrinsic to the ectoderm, whereas polarization of the endoderm may require inductive cues.

*Hydra*'s capacity to self-assemble an intact animal following complete dissociation raises an intriguing question: How does such a remarkable ability evolve, despite the unlikelihood of such catastrophic tissue damage in nature? We found that differences in the preservation of epithelial architecture also occur during wounding of the *Hydra* body column (**Fig. 2.4B, 2.4C**). This raises the possibility that the same mechanisms underlying cell sorting may be broadly elicited for wound healing in *Hydra* and that it may be possible to consider a self-organizing aggregate as a collection of wounds. Notably, the simple sorting mechanism that we describe here facilitates the rapid restoration of ectodermal epithelial integrity, while simultaneously capturing and internalizing any exposed tissues. It is, therefore, tempting to speculate that induction of an

efficient yet simple mechanism for restoring barrier function after wounding may underlie the self-organization of epithelia at the organismal scale in *Hydra*.

Figures and figure legends

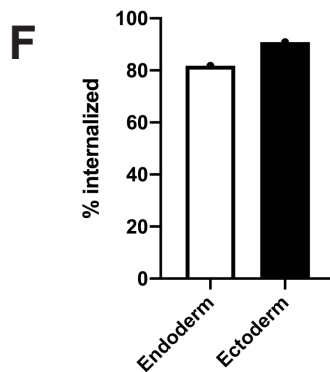
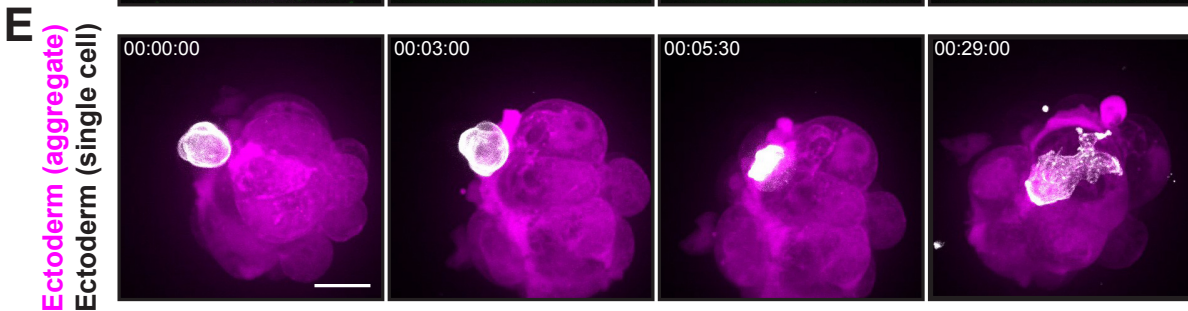
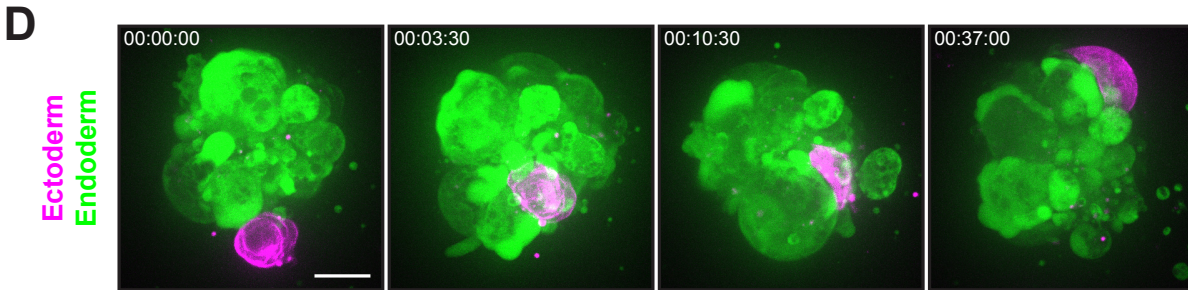
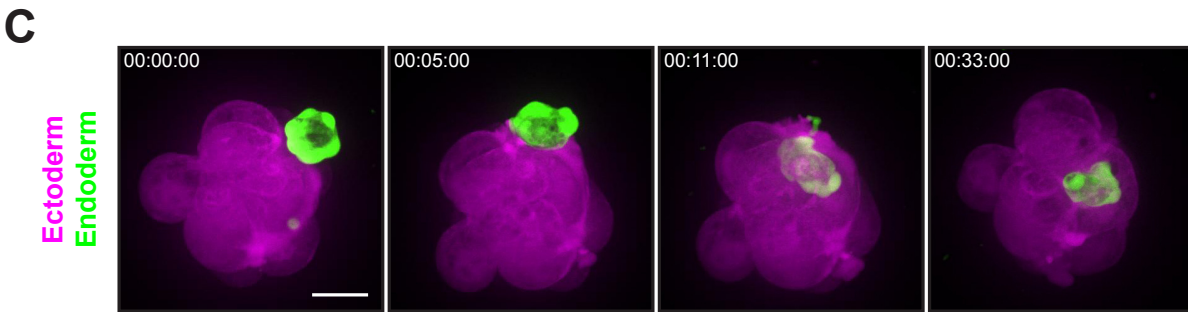
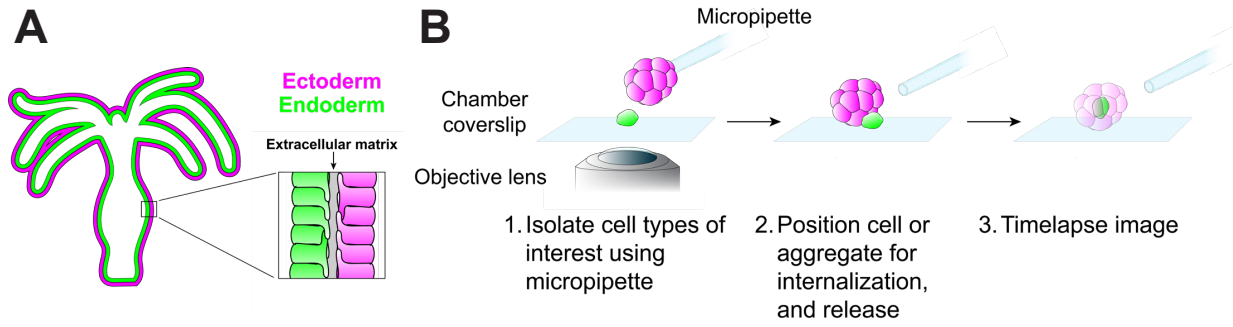
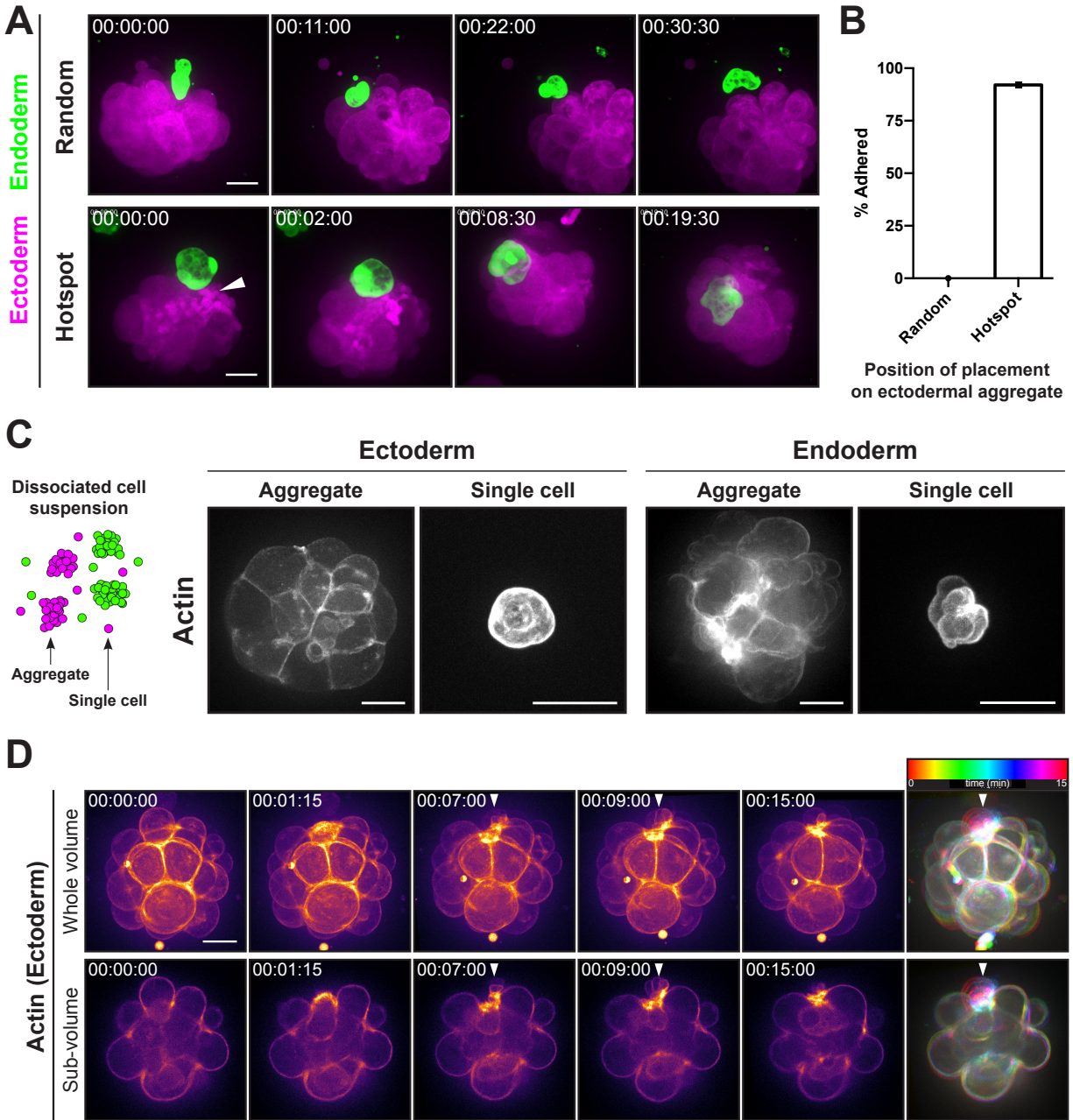


Figure 2.1

**Figure 2.1. Ectodermal aggregates internalize single cells of both epithelial cell types.** A) Schematic of the *Hydra* body plan depicting the organization of ectodermal and endodermal lineages in concentric monolayers. B) Schematic of cell internalization assay using micromanipulation. C) Representative time-course of an ectodermal aggregate expressing DsRed2 (magenta) internalizing a single endodermal cell expressing GFP (green). Quantification is shown in part (F). D) Representative time-course of an ectodermal cell expressing LifeAct-GFP (magenta) adhered to the surface of an endodermal aggregate expressing DsRed2 (green) (n = 10 from 7 independent sample preparations). E) Representative time-course of an ectodermal aggregate expressing DsRed2 (magenta) internalizing a single ectodermal cell expressing LifeAct-GFP (white). Quantification is shown in part (F). (C-E) All frames depict maximum intensity projections of 50–100  $\mu\text{m}$  z-stacks. Timestamps, hh:mm:ss. Scalebars, 20  $\mu\text{m}$ . F) Quantification of the frequency at which single endodermal cells or single ectodermal cells were internalized by ectodermal aggregates (endoderm: n = 11 from 5 independent sample preparations; ectoderm: n = 11 from 10 independent sample preparations). Note that for these experiments, all cells were positioned in contact with hotspots on ectodermal aggregates, as characterized in **Figure 2.2**. See also **Figure S2.1**.





**Figure 2.2. Ectodermal aggregates and internalized entities differ in adhesive properties and multicellular organization.** A) Representative time-courses of ectodermal aggregates expressing DsRed2 (magenta) placed in contact with isolated endodermal cells expressing GFP (green) at either random positions (top) or at hotspots (bottom). Arrowhead denotes hotspot. Due to a lack of adhesion following random placement, aggregates were repeatedly repositioned via micropipette to remain in contact with the endodermal cell. B) Quantification of the frequency of successful adhesion between ectodermal aggregates and endodermal cells within 15 min of placement at either random positions or at hotspots on the ectodermal aggregate surface (Random: n = 12 from 4 independent sample preparations; Hotspot: n = 12 from 5 independent sample preparations). These experiments were performed in parallel with internalization experiments in

**Figure 2.1**, such that hotspot data here include the endodermal internalization data graphed in **Figure 2.1F**. C) Left: Schematic depicting the structures present in dissociated cell suspensions. Right: Representative stills of actin organization in aggregates or single cells expressing LifeAct-GFP ( $n \geq 10$  for all entities depicted). D) Time-course of hotspot formation as a result of epithelial remodeling in a small ectodermal aggregate expressing LifeAct-GFP. Arrowhead denotes a hotspot forming at a site of cell ingress. Bottom panels depict an optical section from the same aggregate. mpl-inferno LUT (FIJI) was applied to aid in visualizing graded LifeAct-GFP signal. Temporal color-coded time-series (right) depicts actin organization and dynamics in the same aggregate. Hotspot (arrowhead) coincides with locally disrupted actin architecture and membrane blebbing. Image registration was used to correct for translation of the aggregate. Images were recorded at 15 s time points. (A-D) All frames depict maximum intensity projections of 50–100  $\mu\text{m}$  z-stacks. Timestamps, hh:mm:ss. Scalebars, 20  $\mu\text{m}$ . See also **Figures S2.2, S2.3**.



internalizing an unlabeled endodermal aggregate. Dashed line indicates the position of the endodermal aggregate (n = 20 from 14 independent sample preparations). B) Left: Schematic of the large aggregate preparation. A suspension of ectodermal and endodermal small aggregates and single cells was pelleted by centrifugation to form large, mixed-lineage aggregates that undergo sorting. Right: Representative time-course of re-epithelialization in a large aggregate generated from animals expressing ectodermal LifeAct-GFP. Dashed line depicts the boundary of a superficial layer of ectodermal cells spreading and fusing to form a continuous epithelium (n = 5 from 4 independent sample preparations). C) Left: Schematic of aggregate manual assembly from isolated cells using micromanipulation. Right: Representative before and after stills of the epithelialization of a manually assembled ectodermal aggregate expressing MRLC-GFP. Acquisition begins after releasing the assembled aggregate from the micropipette (n = 11 from 11 independent sample preparations). D). (A-C) All frames depict maximum intensity projections of 50–100  $\mu\text{m}$  z-stacks. See also **Figure S2.4**. D) Quantification of the number of cells showing epithelial-like morphology and junctional actomyosin localization in manually reassembled ectodermal and endodermal aggregates. Each datapoint represents an individual manually assembled aggregate (ectoderm: n = 11 from 11 independent sample preparations; endoderm: n = 7 from 7 independent sample preparations). The number of epithelialized cells was scored 60 min after manual reassembly. Timestamps, hh:mm:ss. Scalebars, 20  $\mu\text{m}$ .

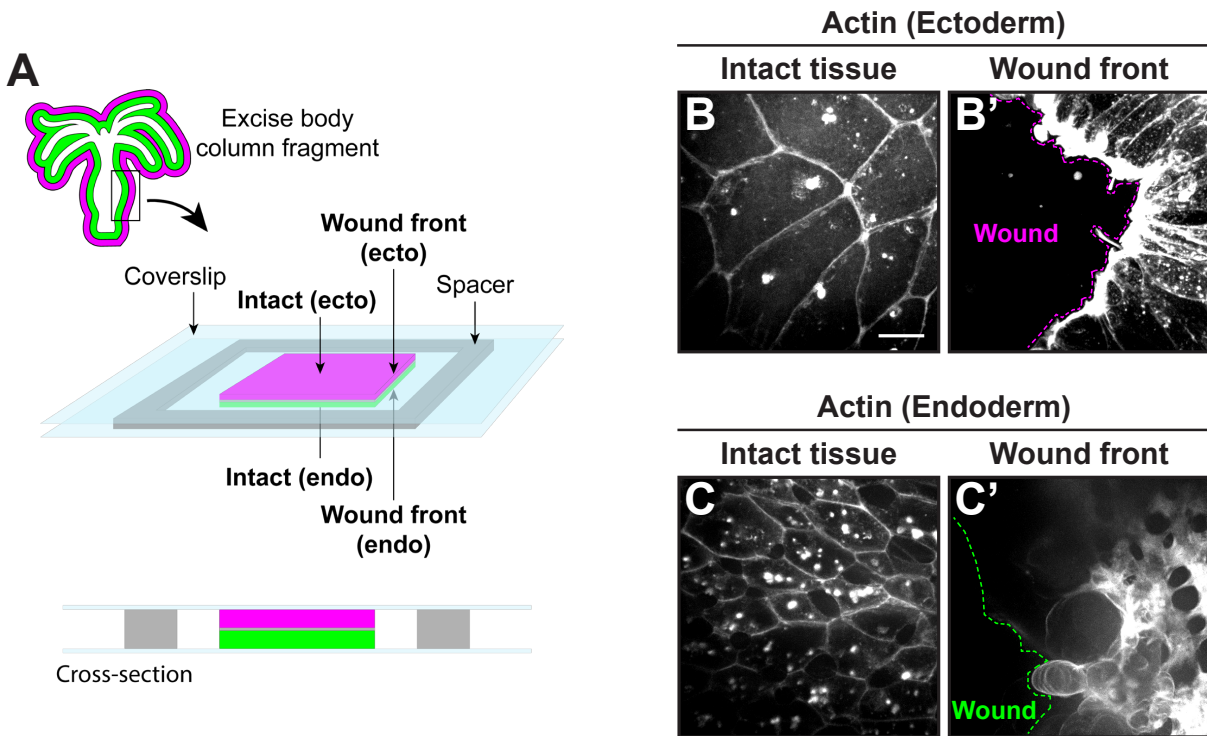


**Figure 2.4. Differential preservation of epithelial architecture occurs upon local wounding.** A) Schematic of wounding assay sample preparation. A living fragment of the body column was excised from the intact animal and sandwiched between coverslips with a 100  $\mu\text{m}$  spacer. Arrows indicate regions of interest for each tissue and region shown in **Figure 2.4B, 2.4C**. B) Representative stills from live imaging of dissected body column fragments expressing LifeAct-GFP in the ectoderm. Imaging was performed at the interior (intact, B) and tissue edge (wound front, B') of the same fragment ( $n = 3$  from 3 independent sample preparations). C) Representative stills from live imaging of dissected body column fragments expressing LifeAct-GFP in the endoderm at the interior (intact, C) and tissue edge (wound front, C') of the same fragment ( $n = 3$  from 3 independent sample preparations). (B-C) Dashed lines indicate the leading edge of the wound front. Intact and wound front images are scaled differently to improve visualization of features. All frames depict maximum intensity projections of 50–100  $\mu\text{m}$  z-stacks. Scalebars, 20  $\mu\text{m}$ .

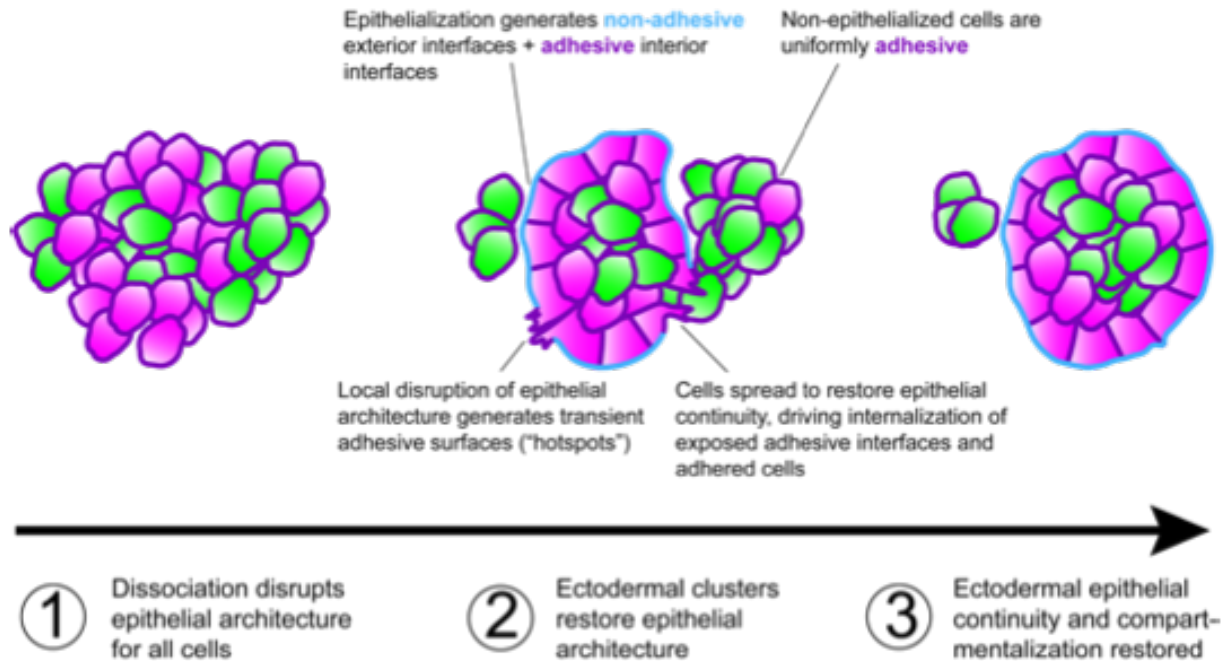


**Figure 2.5. Model of epithelialization-mediated cell sorting in *Hydra*.** Tissue dissociation results in loss of epithelial architecture in both ectodermal and endodermal lineages, rendering them uniformly adherent. Ectodermal aggregates rapidly restore epithelial architecture, generating nonadherent apical surfaces, but preserving adherent interior interfaces. Epithelial discontinuities expose adhesive surfaces from the aggregate interior, allowing them to capture adhesive cells. Adhered cells, along with exposed adhesive interfaces, are internalized as ectodermal cells spread to restore epithelial continuity.

Supplemental figures/tables and legends

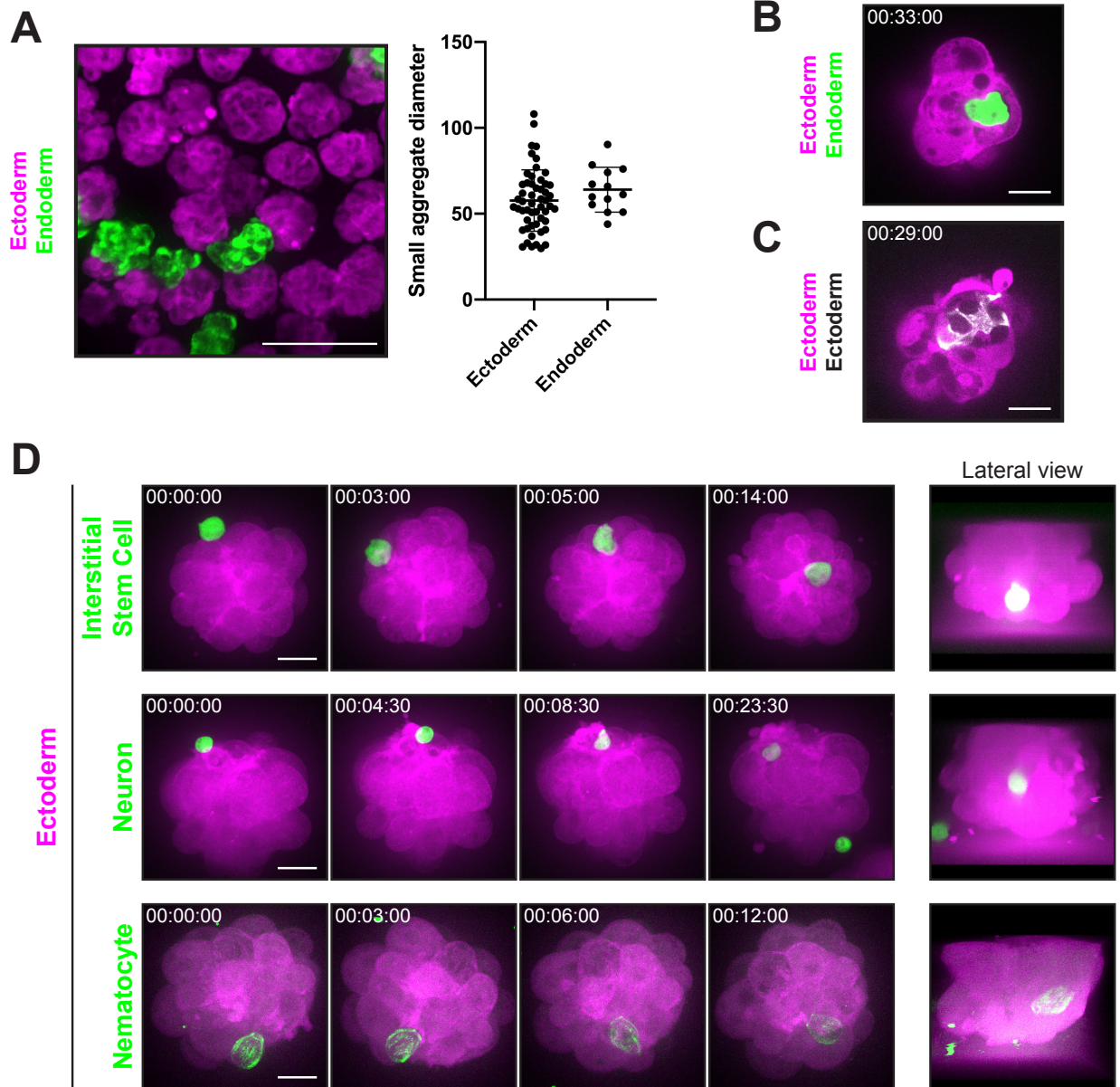


**Figure S2.1. Ectodermal aggregates internalize diverse Hydra cell types, Related to Figure 2.1.** A) Left: Field of view depicting small aggregates isolated via dissociation protocol. Ectodermal aggregates express DsRed2 (magenta). Endodermal aggregates express GFP (green). Right: Quantification of ectodermal and endodermal aggregate diameters (mean  $\pm$  s.d.,  $n = 53$  ectoderm from 7 independent preparations, 13 endoderm from 9 independent preparations). Scalebar, 100  $\mu$ m. B) Optical section of the final timepoint in **Figure 2.1C**, depicting a DsRed2-expressing ectodermal aggregate (magenta) after internalizing a GFP-expressing endodermal cell (green). Section corresponds to a single z-slice at a depth of 21  $\mu$ m from the aggregate surface. C) Optical section of the final timepoint in **Figure 2.1E**, depicting a DsRed2-expressing ectodermal aggregate (magenta) after internalizing a LifeAct-GFP-expressing ectodermal cell (white). Section

corresponds to a single z-slice at a depth of 16  $\mu\text{m}$  from the aggregate surface. D) Representative time-courses of ectodermal aggregates expressing DsRed2 (magenta) internalizing isolated cells of the interstitial cell lineage (green). Top: interstitial stem cells expressing GFP (n = 7/12 internalized from 7 independent sample preparations); middle: neurons expressing GFP (n = 5/5 internalized from 3 independent sample preparations); bottom: nematocytes expressing EB1-GFP (n = 2/2 internalized from 2 independent sample preparations). Lateral views were generated from 3D reconstructions of high-resolution z-stacks recorded after the respective time courses and optically rotated for visualization in the Y-Z plane. For these experiments, coverslips were passivated by Hellmanex III treatment followed by BSA blocking to prevent cell sticking. (B-D) Scalebars, 20  $\mu\text{m}$ . (A-D) Unless specified, all frames depict maximum intensity projections of 50-100  $\mu\text{m}$  z-stacks. Timestamps, hh:mm:ss.



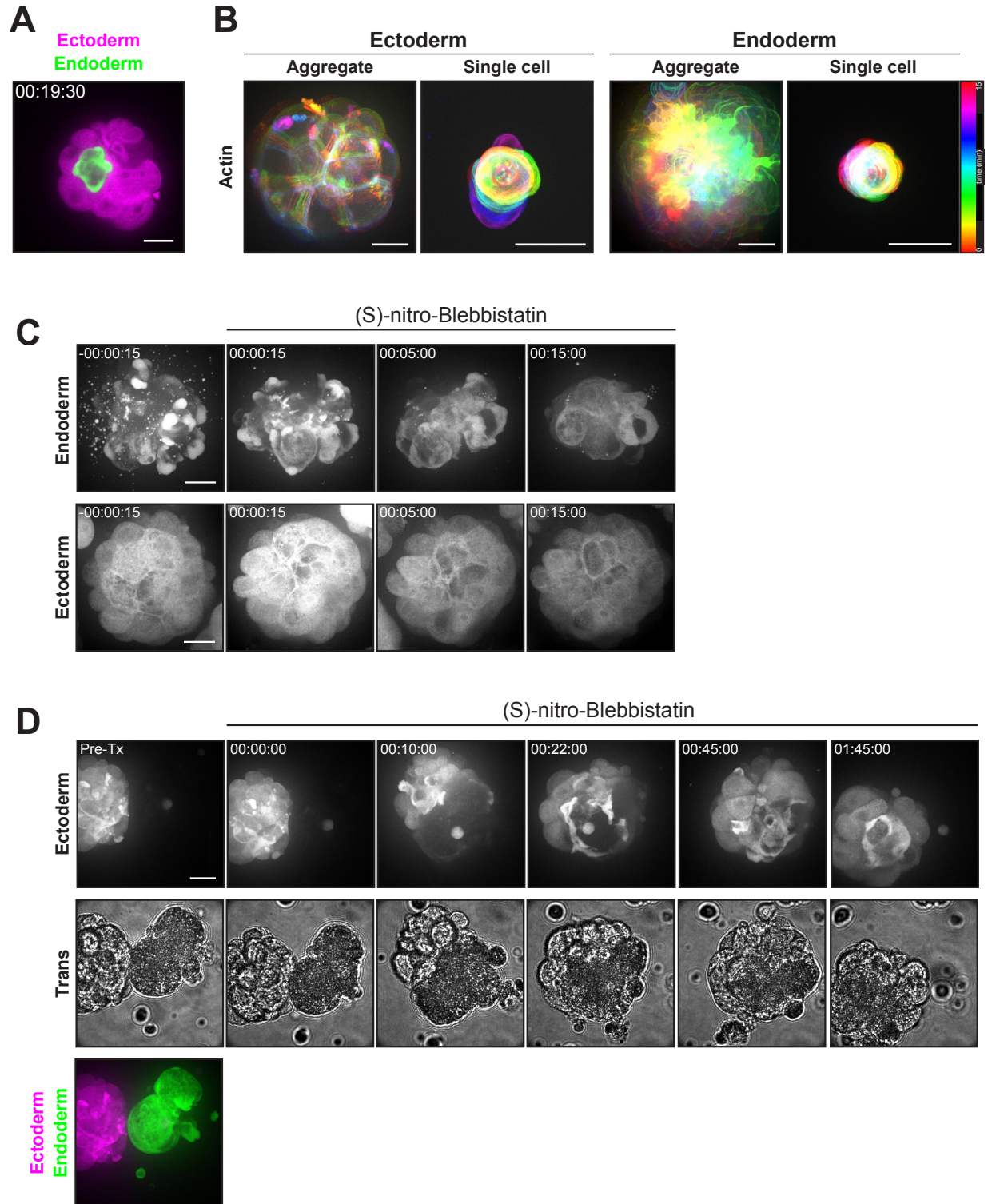


**Figure S2.2. Endodermal blebbing is not essential for internalization, Related to Figure 2.2.**

A) Optical section of the final timepoint in **Figure 2.2A** (bottom), depicting a DsRed2-expressing ectodermal aggregate (magenta) after internalizing a GFP-expressing endodermal cell (green). Section corresponds to a single z-slice at a depth of 21  $\mu\text{m}$  from the aggregate surface. B) Temporal

color-coded time-series depicting the actin organization and dynamics of the aggregates and single cells shown in **Figure 2.2C**. Images were recorded at 15 s time points. C) Representative time-courses of endodermal or ectodermal aggregates treated with 2.5  $\mu\text{M}$  (S)-nitro-Blebbistatin. Aggregates express DsRed2. Time stamp indicates time relative to drug addition. (S)-nitro-Blebbistatin inhibits blebbing in endodermal aggregates, with no observable effect on ectodermal aggregates ( $n = 4$  from 4 independent sample preparations). D) Representative time-course of an ectodermal aggregate expressing DsRed2 internalizing an endodermal aggregate expressing GFP in the presence of 2.5  $\mu\text{M}$  S-Nitro-Blebbistatin. Acquisition began immediately after drug addition. Due to the photoreactivity of S-Nitro-Blebbistatin with blue light, the endoderm (expressing GFP) cannot be imaged after drug addition. Therefore, the endodermal aggregate's position was assessed using transmitted light (trans). A single fluorescent z-stack was taken in both channels before treatment (Pre-Tx) to confirm the identity of aggregates (bottom; ectoderm, magenta; endoderm, green) ( $n = 10$  from 10 independent sample preparations). (B-D) All fluorescence channel frames depict maximum intensity projections of 50-100  $\mu\text{m}$  z-stacks. Transmitted light channel frames depict single z-sections. Timestamps, hh:mm:ss. Scalebars, 20  $\mu\text{m}$ .

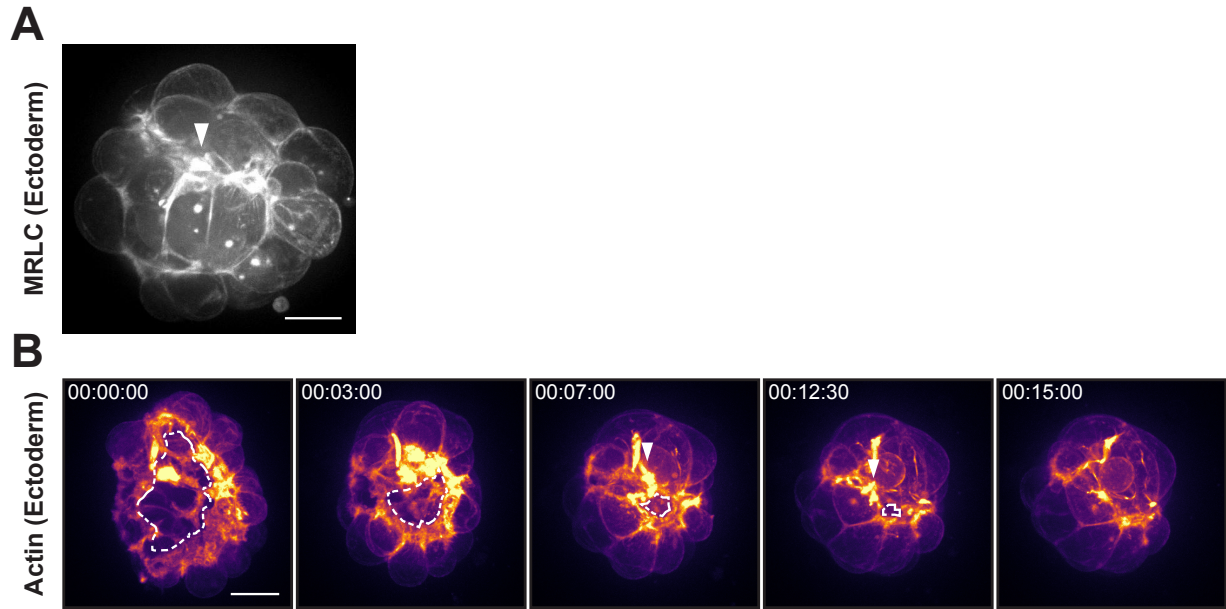


**Figure S2.3. Hotspots emerge at sites of epithelial remodeling, Related to Figure 2.2.** A) Representative still of an ectodermal aggregate expressing MRLC-GFP. Arrowhead indicates hotspot ( $n = 10$  from 10 independent sample preparations). B) Representative time-course of an ectodermal tissue fragment expressing LifeAct-GFP rounding into a spherical aggregate immediately after dissociation. Mpl-inferno LUT (FIJI) was applied to aid in visualizing graded LifeAct-GFP signal. Dashed line indicates fragment edges. Arrowhead denotes a hotspot forming where fragment edges met to establish new cell contacts ( $n = 7$  from 6 independent sample preparations). (A-B) All frames depict maximum intensity projections of 50-100  $\mu\text{m}$  z-stacks. Timestamps, hh:mm:ss. Scalebars, 20  $\mu\text{m}$ .

## Actin (Endoderm)

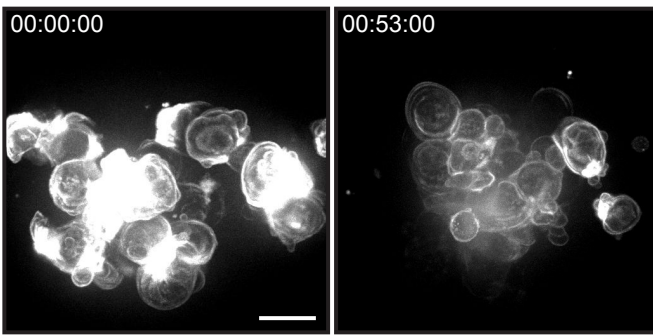


**Figure S2.4. Manually assembled endodermal aggregates fail to restore epithelial architecture, Related to Figure 2.3.** Representative before and after stills of a manually assembled endodermal aggregate expressing LifeAct-GFP. No signs of epithelialization were observed ( $n = 7$  from 7 independent sample preparations; see additional quantification in **Figure 2.3D**). Acquisition began after releasing the assembled aggregate from the micropipette. All frames depict maximum intensity projections of 50-100  $\mu\text{m}$  z-stacks. Timestamps, hh:mm:ss. Scalebars, 20  $\mu\text{m}$ .

## **Materials and methods**

### **Resource Availability**

#### *Lead Contact*

Further information and requests for resources and reagents should be directed to and will be fulfilled by the Lead Contact, Ronald D. Vale (valer@janelia.hhmi.org).

#### *Materials Availability*

Materials generated in this study, including plasmids encoding EB1-GFP and MRLC-GFP, and transgenic *Hydra* expressing MRLC-GFP(ectoderm), are available upon request. The transgenic *Hydra* strain expressing MRLC-GFP(nematocyte) was lost during the course of this study and is, therefore, no longer available.

#### *Data and Code Availability*

No unique code was generated during this study. Source data are available upon request.

## **Experimental Model and Subject Details**

### *Hydra culturing and strains*

*Hydra* were maintained at 18 °C and fed 2-3 times per week with *Artemia* nauplii (Brine Shrimp Direct). Animals were fed  $\geq$  24h prior to dissociation or imaging. Non-budding animals were chosen for experimentation. The following transgenic lines were used for reaggregation and internalization experiments:

DsRed2(ectoderm)/GFP(endoderm) [59]

GFP(ectoderm)/DsRed2(endoderm) [59]

LifeAct-GFP(ectoderm) [47]

LifeAct-GFP(endoderm) [47]

pCnnos1::eGFP (interstitial stem cell reporter) [60]

pActin::GFP(interstitial lineage) (“nGreen,” neuronal reporter) [61]

AEP SS1 (courtesy of Rob Steele)

pActin::EB1-GFP(interstitial lineage) (this manuscript)

pActin::MRLC-GFP(ectoderm) (this manuscript)

### *Generation of transgenic strains*

New transgenic *Hydra* strains were generated as described [23,62]. Predicted homologues of EB1 (t4232aep) and MRLC (t34427aep) were identified by comparing known sequences obtained from UniProt [63] against the *Hydra* 2.0 Genome Project and Juliano aepLRv2 nucleotide databases (<https://research.nhgri.nih.gov/hydra/>) using BLAST (<https://blast.ncbi.nlm.nih.gov>). Coding sequences were cloned from *Hydra* cDNA using primers containing the following sequences:

EB1 Forward: ATGGCAGTAAATGTTTTAATACTGGTGTC

EB1 Reverse: ATATTCATCAGCCTCTCCAGAAATTTCTTCTC

MRLC Forward: ATGTCTTCGAGTAAGAAAACCAAGAAGGG

MRLC Reverse: TTCCTCTTTGGATCCGTGTTTAATGATTC

Coding sequences were subcloned into expression vector pHyVec4 (Addgene ID 34791), between NheI and XmaI restriction enzyme sites. The resulting plasmids (phTS4, phTS5) were injected into 1-4-cell stage *Hydra* embryos of the AEP SS1 strain using a FemtoJet 4i microinjector (Eppendorf), TransferMan 4r micromanipulator (Eppendorf), and dissecting microscope.

## Methodological Details

### *Dissociation and reaggregation*

Dissociation and reaggregation were performed broadly as described [46,64], with some modifications. In brief, ~10-30 animals were incubated at 4 °C for 30-60 min in a filter-sterilized hyperosmotic dissociation medium (DM) pH 6.9-7.0: CaCl<sub>2</sub>•2H<sub>2</sub>O (5 mM), MgSO<sub>4</sub>•7H<sub>2</sub>O (1 mM), KCl (2.8 mM), HEPES (11 mM), Na<sub>2</sub>HPO<sub>4</sub> (0.67 mM), KH<sub>2</sub>PO<sub>4</sub> (0.44 mM), Na Pyruvate (5 mM), Na<sub>3</sub> Citrate•2H<sub>2</sub>O (5 mM), Rifampicin (50 µg/mL). Animals were then dissociated by shear stress by passing through the opening of a glass pipette against the bottom of a 1.5 mL microcentrifuge tube. Animals were sheared in two rounds, first by pipetting ~10 times and discarding the supernatant, adding fresh 4 °C DM, then pipetting ~20-30 times to generate the final cell suspension. After incubating the tube on ice for ~1 min to allow large tissue fragments to settle out of suspension, the supernatant containing single cells and small aggregates was collected. Internalization and adhesion experiments were performed within 3 h of dissociation of a given sample. For internalization assays, single cells and small aggregates of particular cell types were identified by cell type- or lineage-specific fluorescence reporters, isolated by pipette, transferred to imaging chambers, and positioned using the micropipette aspirator (described below). Notably, small aggregates consisted of a single epithelial cell type but maintained some interactions with cells of the interstitial lineage, which are non-fluorescent but can be detected by nuclear staining. To generate large mixed-lineage aggregates, cell suspensions were divided into 150-300 µL volumes (depending on desired aggregate size) and centrifuged at 800 x g for 6 min to pellet. Pelleted samples were incubated on ice for ~5 min to allow aggregates to detach from the tube wall, and aggregates were collected by pipette and transferred to imaging chambers or coverslips.

### *Microscopy and micromanipulation*

Images were acquired on a Yokogawa CSU-X spinning disk confocal attached to an inverted Nikon Ti-E microscope, and Andor iXon Ultra 897 EM-CCD camera (**Fig. 2.2C, S2.2B** single cell ectodermal panel), or a Yokogawa CSU100 spinning disk confocal attached to an inverted Nikon Ti-E microscope, a Hamamatsu C9100-13 EMCCD camera (all other images), all using Micro-Manager software [65]. Z-stacks were acquired at 2-10  $\mu\text{m}$  step sizes for a total depth of 50-100  $\mu\text{m}$ , at 15, 30, or 60 s time intervals, except where higher z-resolution was desired. For higher z-resolution, stacks were acquired at 0.2-1  $\mu\text{m}$  step sizes. All z-stacks were acquired with a 60XA 1.20 NA Plan Apo water immersion objective, with the exception of **Figure S2.1A**, which was acquired with a 20X Plan Apo VC objective. Maximum intensity projections of 50–100  $\mu\text{m}$  Z-stacks are shown throughout, unless otherwise specified.

Imaging chambers were custom assembled from laser cut, rectangular acrylic frames to which coverslips were adhered with vacuum grease (Dow Corning). Micromanipulation experiments used a suction pipette mounted to a Narishige motor-driven micro-manipulator (MM-94) via Narishige microscope mounting adaptor, injection holder, and universal joint (NN-H-4, HI-9, UT-2, respectively). Pipettes were pulled from Sutter Instrument capillary tubes (#B150-110-10) on a Sutter Instrument micropipette puller (P-1000). To achieve the desired opening diameter of 5-10  $\mu\text{m}$ , pulled pipettes were forged on a microforge (MicroData Instruments, Inc. MFG-3). Suction was controlled by adjusting the elevation of a water column or syringe attached to the suction pipette. Single cells of a particular cell type were brought into contact and held until adhesion occurred and then released. Where necessary, LifeAct-GFP-expressing ectodermal cells were distinguished from GFP-expressing endodermal cells by the cell-cortex specific localization of LifeAct-GFP, and the natural pigmentation of endodermal cells visible by transmitted light. To



minimize cell sticking for internalization experiments involving interstitial lineage cell types, coverslips were passivated prior to experimentation by incubation for 1 h in 5% Hellmanex III (Hellma) heated to boiling then maintained at 50 °C. Following Hellmanex treatment, coverslips were washed 10x in deionized water, blocked for 1 h in 4% bovine serum albumin at room temperature, and washed to remove excess BSA.

#### *Drug perturbations*

(S)-nitro-Blebbistatin (Cayman Chemical, Cat #13891) stock solution was prepared in DMSO and diluted directly into imaging chamber dissociation medium to a final concentration of 2.5  $\mu$ M during or immediately preceding acquisition.

#### **Quantification and Statistical Analysis**

Measurements of aggregate sizes were performed in FIJI using the built-in measure function for a line segment drawn along the long axis of aggregates. Measures reflect aggregates that were isolated following small aggregate preparation and do not reflect the complete size distributions for entities found in suspensions, which also contain small cell clusters, single cells, and debris. Successful internalization, as quantified in **Figures 2.1, S2.1** (figure legend), was defined as the complete envelopment of an isolated cell within 1 h after cells adhered to pre-identified hotspots. Successful adhesion, as quantified in **Figure 2.2**, was defined by persistent, unassisted contact between aggregates and isolated cells and their coordinated movement when manipulated by pipette. Aggregates and cells were continuously repositioned to maintain contact for at least 15 min or until adhesion occurred, whichever arose first. “Epithelialized” cells, as quantified in **Figure 2.3**, were defined by the adoption of a flattened and persistent morphology, lack of

blebbing, and local enrichment of actin or myosin at cell junctions. Unless noted, all other images/videos are representative of observations made over all replicates specified in figure legends. Independent preparations specified in figure legends indicate completely independent dissociations and aggregate isolations performed on healthy animals.

### **Acknowledgments**

We thank Iain Cheeseman, Celina Juliano, Ophir Klein, Adam Williamson, Rachel Zwick, Jeff Bush, Abby Kindberg, Sophie Dumont, and members of the Vale laboratory for critical discussions and feedback on the manuscript. We are grateful to Celina Juliano and Rob Steele for numerous insights into *Hydra* care and experimentation and, with Bert Hobmayer and Rafael Yuste, for providing *Hydra* lines and reagents. We thank Vasudha Srivastava for critical discussion and training regarding micromanipulation experiments. This material is based upon work supported by the National Science Foundation Graduate Research Fellowship under Grant No. 1650113 (to TDS). TDS was also supported by the UCSF Chuan Lyu Discovery Fellowship. RDV was supported by the Howard Hughes Medical Institute. KLM was supported by the Damon Runyon Cancer Research Foundation (DRG-2282-17) and by the Eunice Kennedy Shriver National Institute Of Child Health & Human Development of the National Institutes of Health (K99HD101021).

## CHAPTER 3

### Mechanical stretch regulates macropinocytosis in *Hydra vulgaris*

#### Abstract

Cells rely on a diverse array of engulfment processes to sense, exploit, and adapt to their environments. Macropinocytosis is a versatile example of such a process, allowing for the indiscriminate and rapid uptake of large volumes of fluid and membrane. Much of the molecular machinery essential for macropinocytosis has been well established. However, most of these studies relied on tissue culture models, leaving the regulation of this process within the context of organs and organisms unresolved. Here, we report that large-scale macropinocytosis occurs in the outer epithelial layer of the cnidarian *Hydra vulgaris*. Exploiting *Hydra*'s relatively simple body plan, we developed approaches to visualize macropinocytosis over extended periods of time in living tissue, revealing constitutive engulfment across the entire body axis. Using pharmacological perturbations, we establish a role for stretch-activated channels, including Piezo, and downstream calcium influx in inhibiting this process. Finally, we show that the direct application of planar stretch leads to calcium influx and a corresponding inhibition of macropinocytosis. Together, our approaches provide a platform for the mechanistic dissection of constitutive macropinocytosis in physiological contexts and reveal a role for macropinocytosis in responding to membrane tension.

#### Introduction

Engulfment processes are essential for cells to sense and interact with their extracellular environments. In contrast to receptor-mediated endocytosis and phagocytosis, which rely on interactions with specific ligands, macropinocytosis provides a mechanism to indiscriminately engulf large volumes of extracellular fluid and plasma membrane in the absence of a defined target

[66]. This unbiased strategy renders macropinocytosis a highly versatile process, illustrated by the diverse functions it serves (reviewed in [67]), including bulk nutrient acquisition [68,69], immune surveillance [70,71], receptor sequestration [72], and membrane retrieval [73,74]. Regardless of the specific cellular functions served by macropinocytosis, the process involves local remodeling of the actin cytoskeleton to form membrane protrusions, or ruffles, that subsequently fuse to encapsulate extracellular contents. During this process, formation of membrane ruffles depends on the temporally and spatially restricted interactions of phosphoinositides, small GTPases, and actin regulators (reviewed in [75]).

Despite these insights, the factors that initiate macropinocytosis in diverse cell types and physiological contexts are incompletely understood. In some cell types, most notably antigen presenting cells, macropinocytosis occurs constitutively, whereas many other cell types require exogenous growth factor stimulation or pathogen exposure to stimulate macropinocytosis [76,77]. Recent work has identified factors that can enhance the rate of growth factor-mediated macropinocytosis, including excessive cortical localization of the cytoskeleton-membrane linker ezrin [78]. Moreover, recent work in mammalian myotubes revealed that transient reductions in membrane tension following osmotic stress and mechanical stretch can promote growth factor-stimulated macropinocytosis [79,80].

Here, we report the serendipitous discovery of tissue-wide macropinocytosis in the freshwater polyp *Hydra vulgaris*, a representative of the ancestral animal phylum Cnidaria. In contrast to canonical, mammalian models of epithelial macropinocytosis, which require growth factor stimulation (reviewed in [81]), this process unfolds constitutively in *Hydra*'s superficial ectodermal epithelium, accounting for considerable membrane remodeling and fluid uptake. Combining live microscopy with pharmacological perturbations, we establish a role for stretch-

activated channels and  $\text{Ca}^{2+}$  signaling in regulating this process. Finally, by inflating regenerating *Hydra* tissues, we demonstrate a direct role for cellular stretch in regulating macropinocytosis, with high-tension states inhibiting fluid uptake. Together, our findings reveal a role for tissue mechanics in regulating constitutive macropinocytosis and highlight the potential for *Hydra* as a physiological model of macropinocytosis.

## Results

### *Hydra* ectoderm exhibits ubiquitous macropinocytosis

Previous investigations of tissue patterning in *Hydra* have shown that the actin reporter LifeAct-GFP localizes to actin-enriched basal myonemes and apical cell junctions of the outer (ectodermal) epithelium [47,82]. In our studies, we also observed that LifeAct-GFP labeled dynamic, ring-shaped structures that localized to the apical cell membrane (**Fig. 3.1A**). Phalloidin staining in fixed, intact animals confirmed that these structures were enriched for actin (**Fig. 3.1B**). These actin-rich rings were found at a low frequency along the entire body plan (**Fig. S3.1**) and bore a striking resemblance to structures identified in classic scanning electron microscopy of the *Hydra* ectoderm [83]. Since *Hydra* display considerable contractile movement in three-dimensions, we developed a preparation that would allow us to better monitor the dynamics of the actin rings over extended periods. This preparation involved amputating the head and foot from animals and threading the resulting body columns onto filaments to roughly constrain tissue movement to a single plane (**Fig. 3.1C**). This approach allowed us to capture the entire lifecycle of actin rings, which formed as an expanding ring, reaching a diameter of  $10.49 \pm 2.6 \mu\text{m}$  ( $n = 35$  from 3 independent preparations), and then constricted to a focus and ultimately disappeared (lifespan:  $109 \pm 32 \text{ s}$ ;  $n = 35$  from 3 independent preparations; **Fig. 3.1D**).

Given their resemblance to circular dorsal ruffles and macropinocytic cups in mammalian cells [84] (reviewed in [85]), we considered whether the ring structures may play a role in fluid uptake. To test this, we incubated the threaded body columns in media containing fluorescently labelled dextran. As rings formed, dextran accumulated in the resulting invaginations and was engulfed upon ring constriction (**Fig. 3.1E**). The resulting dextran-filled vacuoles persisted within ectodermal cells and accumulated in the tissue over time (**Fig. 3.1F, 3.1G**). Thus, the actin rings denote macropinocytic cups associated with fluid uptake.

### **Stretch-activated channel activity regulates macropinocytosis**

Intriguingly, we observed a trend of more macropinocytic cups in isolated *Hydra* body columns ( $0.186 \pm 0.140$  cups per cell;  $n = 4$  independent preparations) when compared to fixed, intact animals ( $0.015 \pm 0.011$  cups per cell;  $n = 15$  from 3 independent preparations). Moreover, the frequency of macropinocytic cups increased over time in body columns following amputation (**Fig. 3.2A**). As the incisions required for head and foot amputation are likely to affect tension in the epithelium, we considered whether tissue mechanics may play a role in regulating macropinocytosis.

Stretch-activated channels play a role in tension sensing in a variety of biological contexts [86], and analysis of recent *Hydra* single-cell RNA sequencing data [61] revealed that the *Hydra* ectoderm expresses several putative TRP (e.g. t27236aep, t29007aep) and Piezo (t21136aep) channel proteins that may contribute to mechanosensation. To determine if stretch-activated channels modulate macropinocytic cup formation, we treated *Hydra* with gadolinium chloride ( $\text{GdCl}_3$ ), a broad-spectrum inhibitor of these channels [87]. Immunofluorescence and live imaging in intact animals revealed a striking increase in macropinocytic cups following treatment with

GdCl<sub>3</sub> (50 μM; **Fig. 3.2B, 3.2C, S3.2A**). We observed no significant increase in the frequency of macropinocytotic cups in GdCl<sub>3</sub>-treated threaded body columns over their already elevated levels of macropinocytosis (**Fig. S3.2B**), suggesting that the effect observed in this preparation may indeed result from mechanical unloading. To further probe the role of stretch-activated channels, we performed the reciprocal experiment of treating *Hydra* body columns with Jedi1 and Jedi2, which are activators of the stretch-activated channel Piezo1 [88]. Treatment with either Jedi drug resulted in a near complete, albeit transient, depletion of macropinocytotic cups in isolated body columns, coinciding with contraction of the tissue (**Fig. 3.2D, 3.2E, S3.2C**). Together, these findings implicate stretch-activated channels, including Piezo1, in the regulation of macropinocytosis in *Hydra*.

Upon activation, stretch-activated channels signal mechanical stimuli through the transport of ions, predominantly Ca<sup>2+</sup> influx in the case of Piezo channels [89]. To directly monitor calcium flux in the *Hydra* ectoderm, we prepared threaded body columns from transgenic *Hydra* expressing the fluorescent calcium reporter GCaMP6s in ectodermal tissues [90]. Intriguingly, we observed a gradual decrease in fluorescence intensity as body columns conformed to their filaments (**Fig. 3.2F, 3.2G, S3.2D**), coinciding with the period of increasing macropinocytosis reported above. Treatment of body columns with Jedi1 or Jedi2 induced a transient spike in GCaMP6s fluorescence, accompanied by strong contractions (**Fig. 3.2F, 3.2G, S3.2D**).

To further test the extent to which Jedi1/2 inhibited macropinocytosis via changes in intracellular calcium, we treated threaded *Hydra* body columns with ionomycin to promote stretch-activated channel-independent calcium influx. Using GCaMP6s-expressing *Hydra*, we confirmed that ionomycin induced an increase in fluorescence intensity and body column contractions, indicating an increase in cytosolic calcium concentrations (**Fig. 3.2G, S3.2D**). In LifeAct-GFP-

expressing body columns, ionomycin treatment resulted in a transient decrease in macropinocytic cups. Intriguingly, this effect was less pronounced and shorter lived than that observed upon exposure to Jedi1 or Jedi2 (**Fig. 3.2D, 3.2E**), despite a greater and more sustained calcium influx following ionomycin treatment (**Fig. 3.2G**). Thus, while our findings suggest that calcium influx is sufficient to transiently inhibit macropinocytosis, this alone may not explain the magnitude of the effect observed following Piezo1 activation.

### **Mechanical stretch inhibits macropinocytosis**

In light of our data implicating stretch-activated channels in regulating macropinocytosis, we sought to directly test the effects of tissue stretch on this process. Body column fragments that are allowed to heal (i.e. without threading onto filaments) form hollow tissue spheres, which undergo cycles of swelling and rupturing and are capable of ultimately regenerating healthy *Hydra* [91,92]. We sought to capitalize on the architectural simplicity and deformability of these regenerating “spheroids” as a system for applying stretch. To this end, we microinjected *Hydra* medium into the lumen of *Hydra* spheroids, inflating them to approximately 1.5 times their original volume before they ruptured (approximated volume fold change:  $1.47 \pm 0.19$ ; **Fig. 3.3A, S3.3**). In an inflated state, ectodermal cells of LifeAct-GFP-expressing spheroids exhibited enlarged apical surface areas, suggestive of a planar ectodermal stretch (**Fig. 3.3B**).

We next characterized the abundance of macropinocytic cups in inflated and uninflated LifeAct-GFP-expressing spheroids. Macropinocytic cups were depleted in inflated aggregates when compared to their pre-inflation states. As aggregates gradually deflated following needle removal, we observed a recovery of macropinocytosis (**Fig. 3.3B, 3.3C**). Applying the same protocol to GCaMP6s-expressing spheroids, we observed a dramatic increase in GCaMP6s



fluorescence during spheroid inflation. As spheroids deflated, GCaMP6s fluorescence gradually diminished to basal levels (**Fig. 3.3D, 3.3E**). Needle insertion and removal also resulted in brief spikes in GCaMP6s intensity (**Fig. 3.3E**). However, mock inflations, in which a microinjection needle was inserted into spheroids for a comparable duration without inflation, did not significantly affect macropinocytosis (**Fig. 3.3C**). Together these data indicate that inflation of spheroids, with an accompanying stretch of the epithelial layer, leads to calcium influx and inhibits macropinocytosis.

## **Discussion**

Here, we describe widespread macropinocytosis in the outer epithelium of *Hydra vulgaris*. Our results suggest that this phenomenon is regulated by tension applied to the epithelial layer. This is most directly demonstrated by the finding that inducing stretch in *Hydra* spheroids through inflation is sufficient to transiently inhibit macropinocytosis, with macropinocytosis rapidly recovering following deflation and relaxation of spheroids. This tissue stretch coincides with a rise in intracellular calcium in epithelial cells. We further show that pharmacological inhibition of ion flux through stretch-activated channels results in the activation of macropinocytosis and that Piezo1 activation or calcium ionophores repress macropinocytosis. Together, our findings highlight a role for tissue mechanics and stretch-activated channels in the regulation of macropinocytosis in *Hydra* (**Fig. 3.4**).

Macropinocytosis is historically categorized as “constitutive” or “stimulated,” based on the requirement for growth factors for ruffle induction. Constitutive macropinocytosis has been attributed to relatively few cell types, most notably, amoebae and antigen presenting cells, where respective roles in feeding and immune surveillance have been described (reviewed in [93,94]). In

contrast, most mammalian epithelial models for which macropinocytosis has been reported require growth factor stimulation. Given that macropinocytosis in *Hydra* occurs in a wide variety of culture conditions without supplementation, our findings likely reflect an underappreciated form of constitutive epithelial macropinocytosis. Intriguingly, a similar ubiquitous macropinocytosis was recently reported in the tissues of other cnidarian species [95], raising the possibility that constitutive macropinocytosis is more widespread than previously appreciated, at least among basal metazoans.

Our findings directly implicate membrane tension as a regulator of macropinocytosis, expanding the repertoire of exogenous effectors beyond growth factors [77] and pathogens [76]. Precisely how properties like membrane tension may contribute to macropinocytosis remains unresolved. Membrane tension may be transduced to biochemical signals that limit actin nucleation and membrane protrusion. A similar mechanical-biochemical crosstalk has been described in the actin-mediated migration of neutrophils [96,97]. Alternatively, macropinocytic cups may form and evolve more readily in low-tension conditions, as the energetic cost to deform membranes may be reduced [98]. While we cannot exclude the latter possibility, our finding that the pharmacological inhibition of stretch-activated channels is sufficient to induce macropinocytosis suggests an active contribution.

In our experiments, gadolinium, which broadly inhibits stretch-activated channels, promoted macropinocytosis. Moreover, application of the Piezo-specific activators Jedi1/2 [88] resulted in a transient inhibition of macropinocytosis, accompanied by calcium influx and tissue contraction. This indicates a role for, but not limited to, Piezo channels in macropinocytosis regulation. Piezo function has been extensively explored in epithelia, where Piezo1 indirectly senses cellular crowding via membrane tension to maintain homeostatic cell densities [99,100].

Intriguingly, recent work similarly identified Piezo1 as a regulator of epidermal growth factor-stimulated macropinocytosis in cancer cells [101]. In mammalian myotubes, where a role for membrane tension in macropinocytosis has also been reported, tension-mediated redistribution of phospholipase D2 in the plasma membrane was proposed to promote actin remodeling and membrane ruffling, suggesting an alternative mechanisms to transduce mechanical stimuli to biochemical signals [79,80]. Thus, tissue stretch may play a role in macropinocytosis in a number of contexts, and whether additional factors beyond stretch-activated channels contribute to this process in *Hydra* remains to be determined.

Stretch-activated channels provide a means to transduce mechanical stimuli to chemical signals by conducting ions across the plasma membrane [89]. Using ionomycin to induce calcium influx independent of stretch-activated channels, we observed a lesser and more transient inhibition of macropinocytosis when compared to treatment with Piezo1 activators Jedi1/2. Piezos are non-selective cation channels permeable to a number of ions in addition to  $\text{Ca}^{2+}$ , including  $\text{K}^+$ ,  $\text{Na}^+$ , and  $\text{Mg}^{2+}$ , all of which are present in *Hydra* medium and may, therefore, explain some of the observed effect of Piezo activation [102]. Alternatively, it is conceivable that the robust and sustained depolarization that occurs in the presence of ionomycin interferes with the mechanisms required to inhibit macropinocytosis. Future studies will provide further insight into the requirements for macropinocytosis and its inhibition in *Hydra*.

Although both our pharmacological and physical perturbations indicate a role for stretch in inhibiting macropinocytosis, we note several reasons for caution in interpreting these findings. For instance, calcium influx causes contraction of *Hydra*'s epithelial myonemes, which may, in turn, alter tension at the apical membrane. Thus, while Jedi1/2 and ionomycin treatment transiently inhibited macropinocytosis, these effects may be an indirect consequence of contraction, rather

than a direct effect of Piezo activation. Further genetic analysis will be useful in dissecting the mechanistic roles of Piezo channels and calcium signaling in macropinocytosis in *Hydra*. Additionally, amputated and isolated body columns provide an unparalleled opportunity to observe macropinocytosis but require substantial tissue wounding, which may contribute to the influx of macropinocytotic cups we observe in this context. Nevertheless, our spheroid inflation approach circumvents acute injury on this scale and provides the most direct evidence for tissue mechanics in the regulation of macropinocytosis.

The role of macropinocytosis in *Hydra* remains unknown. Given *Hydra*'s predatory feeding behaviors, macropinocytosis is unlikely to play a significant role in nutrient acquisition. Similarly, the dilute solutes available in *Hydra*'s freshwater habitats likely render this process inefficient for acquiring or responding to dissolved environmental factors. Alternatively, macropinocytosis may contribute to the uptake and remodeling of contents already associated with the animal's surface. Notably, *Hydra* epithelia have been shown to internalize particles of various sizes, including beads of up to 1  $\mu\text{m}$  in diameter [26,103], which demonstrates an ability to indiscriminately engulf solid substrates that may be explained by our findings. In one study [103], ultrastructural analysis revealed large, nanoparticle-filled vacuoles containing remains of the *Hydra* "cuticle," a fibrous structure secreted by and surrounding *Hydra*'s apical ectodermal surface and home to a complex microbial community [104–106]. Thus, macropinocytosis may provide an efficient means to remodel the *Hydra* cuticle and sense and respond to the microbiome.

Given our data showing stretch-sensitivity, we also speculate that macropinocytosis could play a role in regulating membrane tension through the removal of large regions of the apical plasma membrane. The *Hydra* epithelium is a remarkably dynamic tissue, characterized by perpetual growth and cell loss, extensive cellular rearrangements [107] (reviewed in [108]), and

drastic changes in aspect ratio during animal contraction and elongation. Based on measurements of macropinocytic cup size and macropinosome accumulation, we estimate rates of membrane retrieval in isolated body columns exceeding  $150 \mu\text{m}^2$  per min per  $10,000 \mu\text{m}^2$ , corresponding to complete apical membrane turnover in approximately 1 h. Thus, our findings suggest a significant capacity for membrane recycling through macropinocytosis. Together with the regulatory role for cellular stretch that we identify, it is tempting to speculate that this capacity to rapidly recycle apical membrane may contribute to maintaining membrane tension and remodeling tissues. Although we did not observe direct evidence for such a mechanism, this may be confounded by comparable rates of membrane deposition in isolated body columns, as we observed no apparent decreases in apical membrane surface area during this process. Future efforts to uncouple membrane retrieval and deposition may shed light on a role for macropinocytosis in membrane tensioning and, more broadly, reveal the contributions of tension-regulated macropinocytosis to *Hydra* physiology.

Figures and figure legends

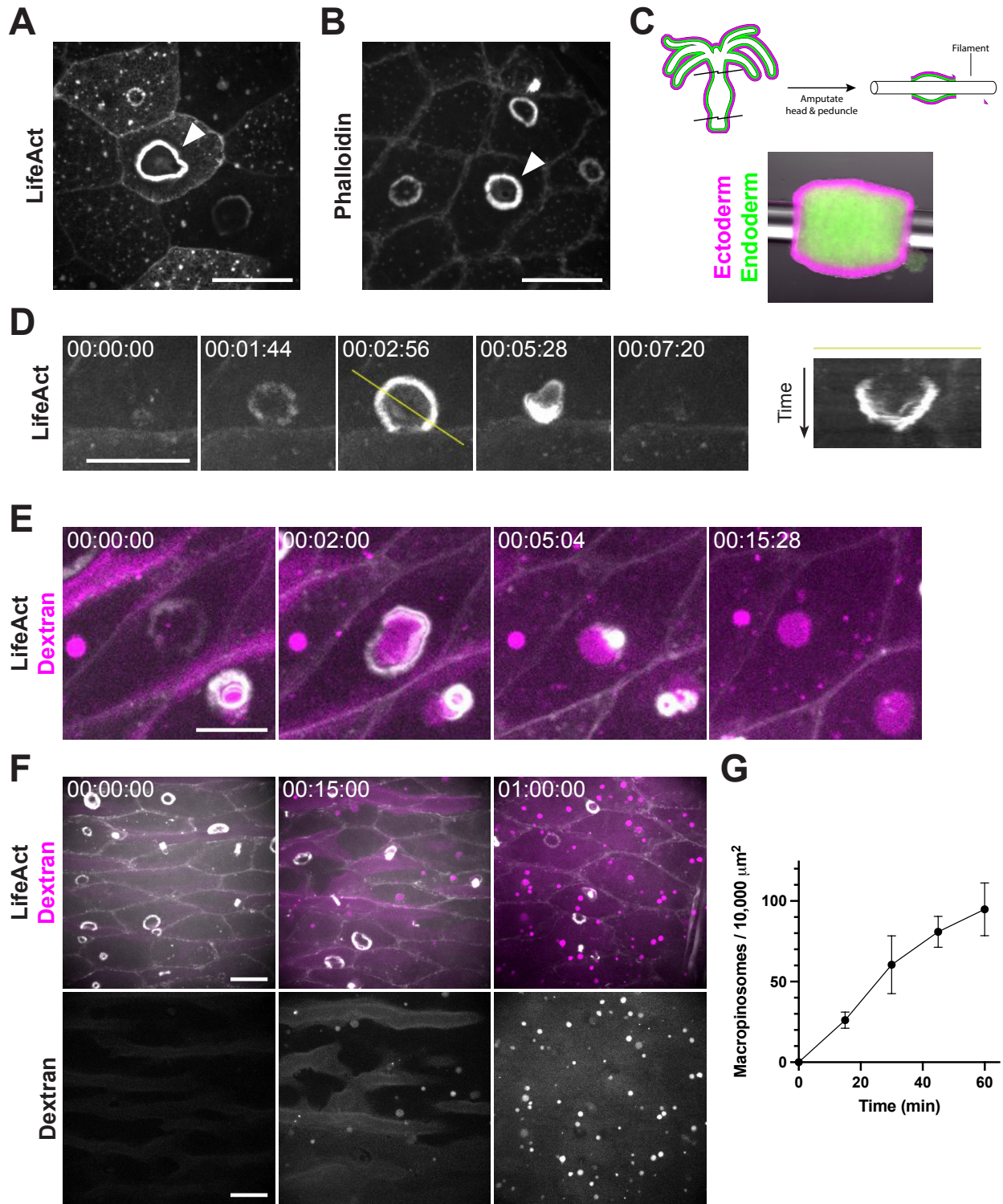


**Figure 3.1. *Hydra* ectoderm exhibits ubiquitous macropinocytosis.** A) Representative image of macropinocytic cups (arrowhead) in the ectoderm of a live, LifeAct-GFP-expressing *Hydra*. B) Representative image of macropinocytic cups (arrowhead) in the ectoderm of a fixed *Hydra*

stained with phalloidin. C) Schematic (top) and representative image (bottom) of the body column isolation preparation used for prolonged live imaging. Ectodermal and endodermal cells express DsRed2 (magenta) and GFP (green), respectively. D) Representative time-course of macropinocytic cup formation, closure, and dissipation, visualized by LifeAct-GFP (left). Image registration was performed to compensate for translational movement in the body column. Yellow line denotes the axis of the corresponding kymograph showing the complete lifecycle (right). E) Representative time-course of fluorescently labeled dextran (magenta) engulfment by macropinocytic cups, visualized by LifeAct-GFP (white). Image registration was performed to compensate for translational movement in the body column. F) Representative time-course of dextran-filled macropinosome (magenta) accumulation in ectodermal tissues expressing LifeAct-GFP (white). Dextran channel is isolated at (bottom). G) Quantification of dextran-filled macropinosome accumulation (mean  $\pm$  sd; n = 3 independent sample preparations). (A–F) All frames depict maximum intensity projections of 10–35  $\mu$ m z-stacks. Time stamps, hh:mm:ss. Scale bars, 20  $\mu$ m. (D–F) All time-courses depict isolated, threaded body columns.

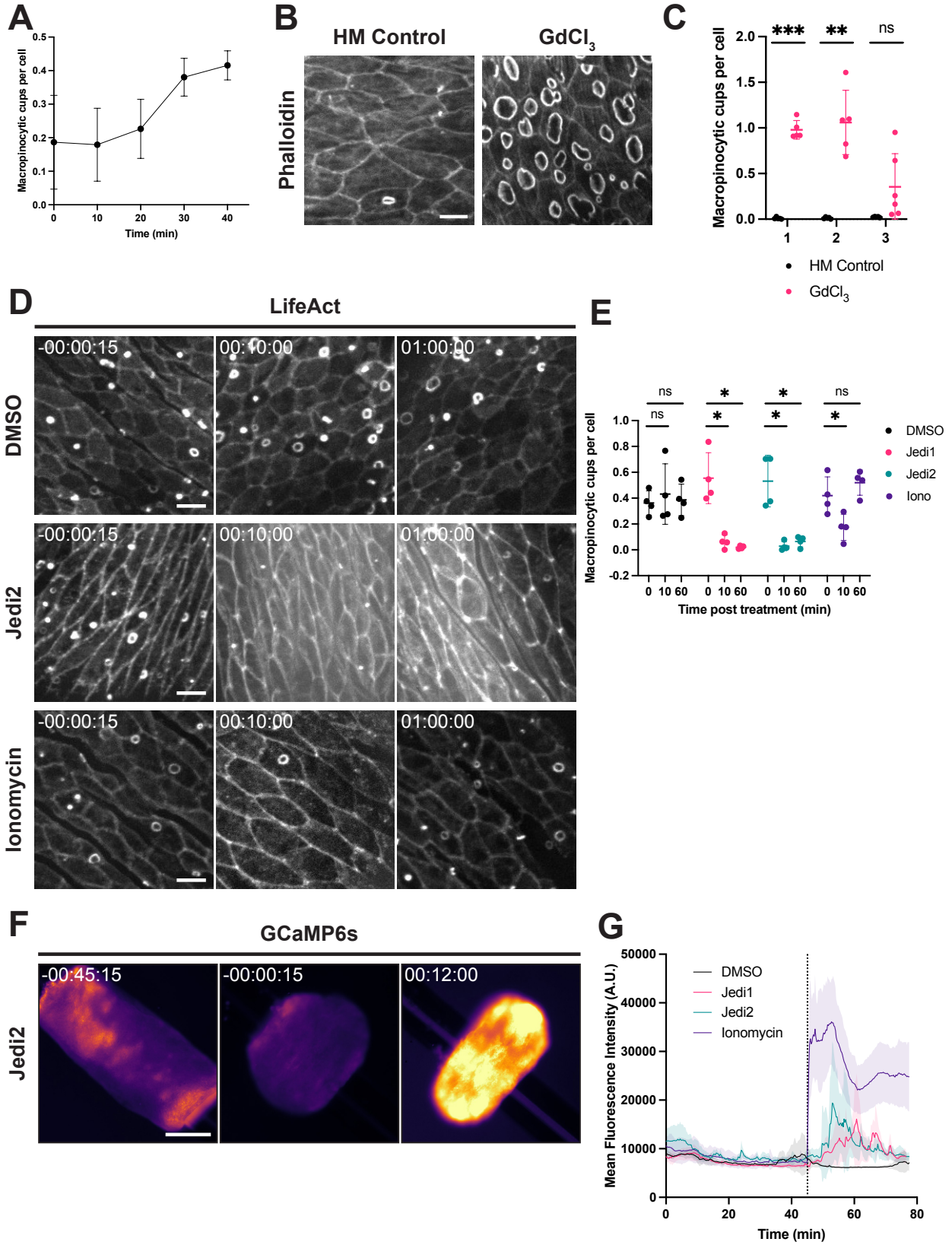
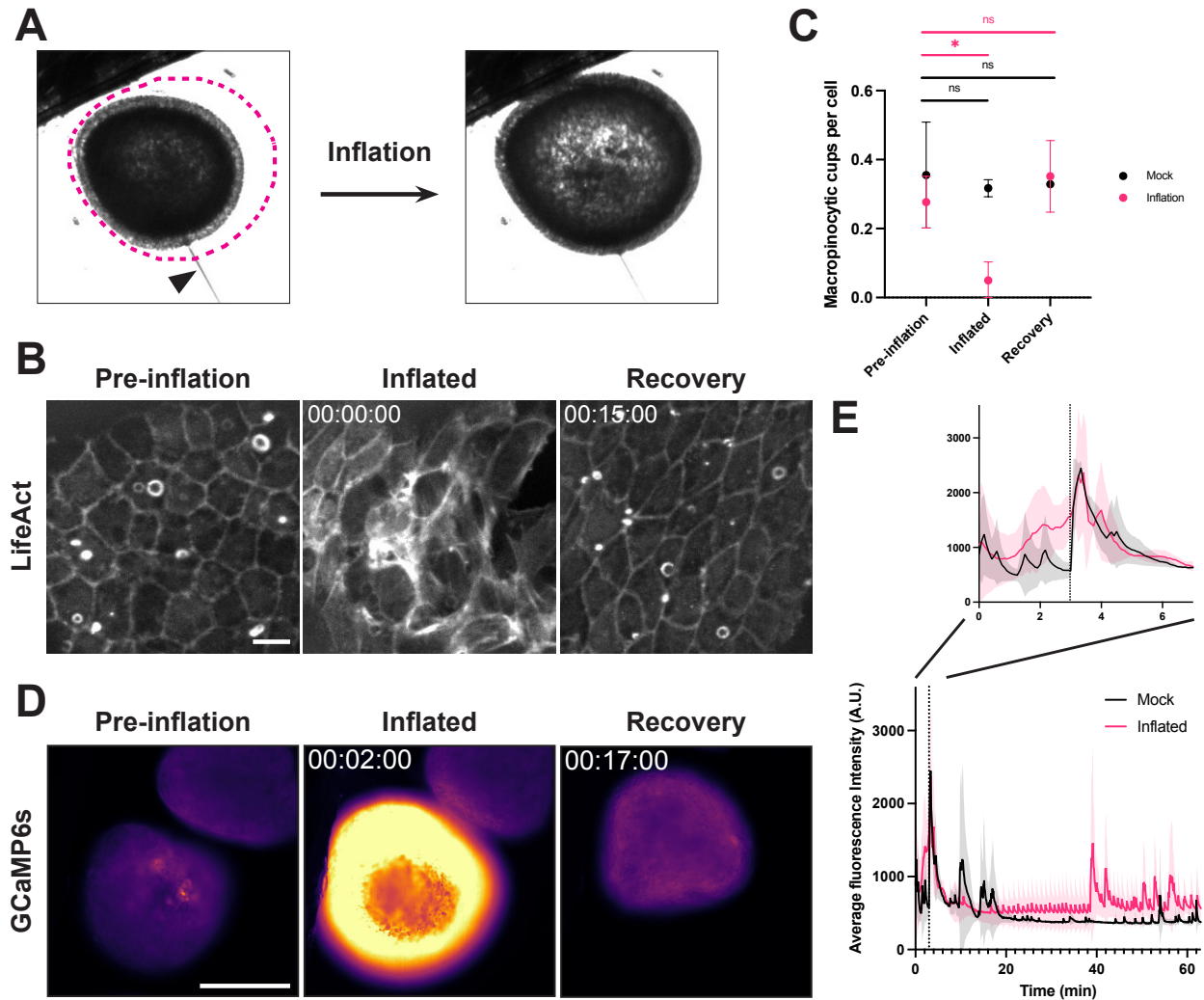


Figure 3.2



**Figure 3.2. Stretch-activated channel activity regulates macropinocytosis.** A) Quantification of macropinocytic cup abundance over time in threaded body columns (mean  $\pm$  sd; n = 4 independent sample preparations). t = 0 min corresponds to the earliest acquirable time point after body column amputation and threading. B) Representative images of macropinocytic cups stained with phalloidin in *Hydra* medium (HM) control (left) and GdCl<sub>3</sub>-treated (right; 50  $\mu$ M for 15 min) intact *Hydra*. Scale bar, 20  $\mu$ m. C) Quantification of macropinocytic cup frequency in response to specified treatments shown in (B). 3 Independent sample preparations are shown per condition (Bars: mean  $\pm$  sd; n  $\geq$  5 animals per condition per independent sample preparation; ns = not significant, \*\* = p < 0.01, \*\*\* = p < 0.001, Student's t-test). D) Representative time-courses of threaded body columns expressing LifeAct-GFP in the ectoderm before (left) and after (center, right) treatment with DMSO, Jedi2 (200  $\mu$ M), or ionomycin (10  $\mu$ M). Scale bars, 20  $\mu$ m. E) Quantification of macropinocytic cup frequency before, 10 min after, and 1 h after specified treatments shown in (D) (Bars: mean  $\pm$  sd; n = 4 independent sample preparations per condition; ns = not significant, \* = p < 0.05, Student's t-test). See also **Figure S3.2C**. F) Representative time-course of a threaded body column expressing GCaMP6s in the ectoderm, before (left, center) and after (right) Jedi2 treatment (200  $\mu$ M). Images represent single z-sections. mpl-inferno LUT (FIJI) was applied to aid in visualizing graded GCaMP6s signal. Scale bar, 500  $\mu$ m. G) Traces depicting mean fluorescence intensity over time in threaded body columns before and after specified treatment (line and shading: mean  $\pm$  sd; n = 4 independent sample preparations per condition). Dotted line indicates drug or vehicle addition. See also **Figure S3.2D**. (B, D) All frames depict maximum intensity projections of 15–35  $\mu$ m z-stacks. (D, F) Time stamps indicate time relative to drug addition; hh:mm:ss.



**Figure 3.3. Application of tissue stretch inhibits macropinocytosis.** A) Representative images of the same *Hydra* spheroid before (left) and after inflation (right). Magenta trace indicates the profile of the spheroid at peak inflation. Arrowhead: microinjection needle. B) Representative time-course of the same spheroid expressing ectodermal LifeAct-GFP before (Pre-inflation), immediately after inflation and needle removal (Inflated), and during recovery (Recovery). Time stamp indicates time relative to needle removal following inflation; hh:mm:ss. All frames depict maximum intensity projections of 15–35  $\mu\text{m}$  z-stacks. Pre-inflation and Inflated/Recovery images have been scaled independently to compensate for an increase in signal following inflation. Scale bar, 20  $\mu\text{m}$ . C) Quantification of macropinocytic cup frequency during inflation experiments shown in (B) (mean  $\pm$  sd;  $n = 3$  independent sample preparations per condition; ns = not significant, \* =  $p < 0.05$ , Student's t-test). D) Representative time-course of the same spheroid expressing ectodermal GCaMP6s before (Pre-inflation), immediately after inflation (Inflated), and during recovery (Recovery). mpl-inferno LUT (FIJI) was applied to aid in visualizing graded GCaMP6s signal. Time stamp indicates time relative to initiation of inflation; hh:mm:ss. All frames depict single z-sections. Scale bar, 200  $\mu\text{m}$ . E) Traces depicting mean GCaMP6s fluorescence intensity over time during inflation experiments (line and shading: mean  $\pm$  sd;  $n = 3$  independent sample preparations per condition). Dotted line indicates needle removal.

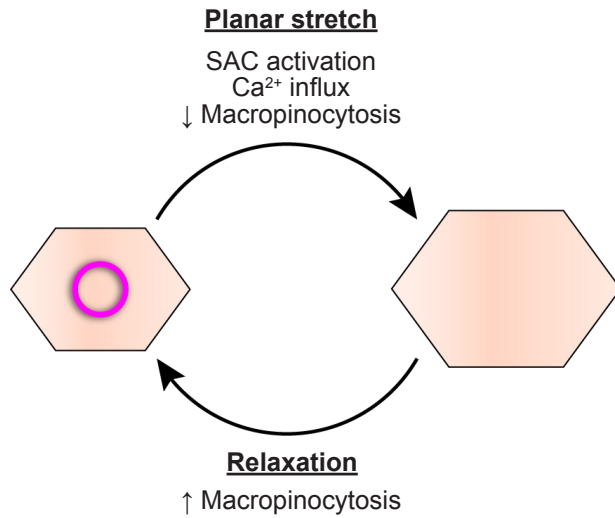


**Figure 3.4. Mechanical stretch-regulated macropinocytosis.** Model of mechanically regulated macropinocytosis in *Hydra*. Planar stretch results in stretch-activated channel (SAC) activation, calcium influx, and inhibition of macropinocytosis. Following tissue relaxation, SAC inactivation restores macropinocytosis.

## Supplemental figures/tables and legends

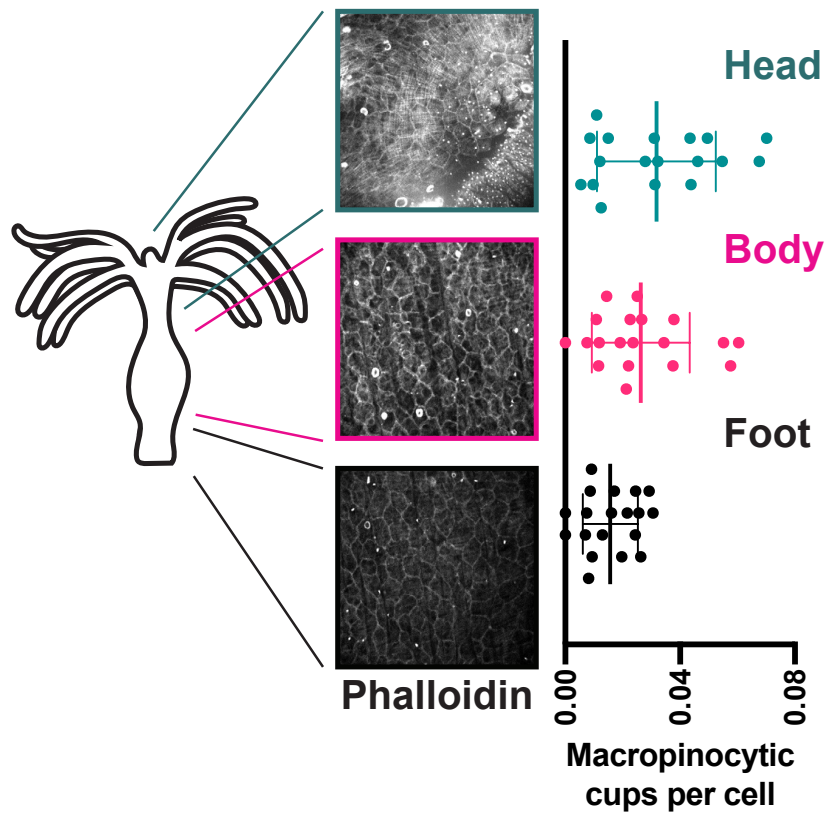


**Figure S3.1.** Schematic (left), representative images (middle), and quantification (right) of macropinocytic cup abundance in the head, body column, and foot of fixed, intact *Hydra* stained with phalloidin (mean  $\pm$  sd;  $n \geq 18$  animals from 3 independent sample preparations per body region). All frames depict maximum intensity projections of 10–35  $\mu\text{m}$  z-stacks.

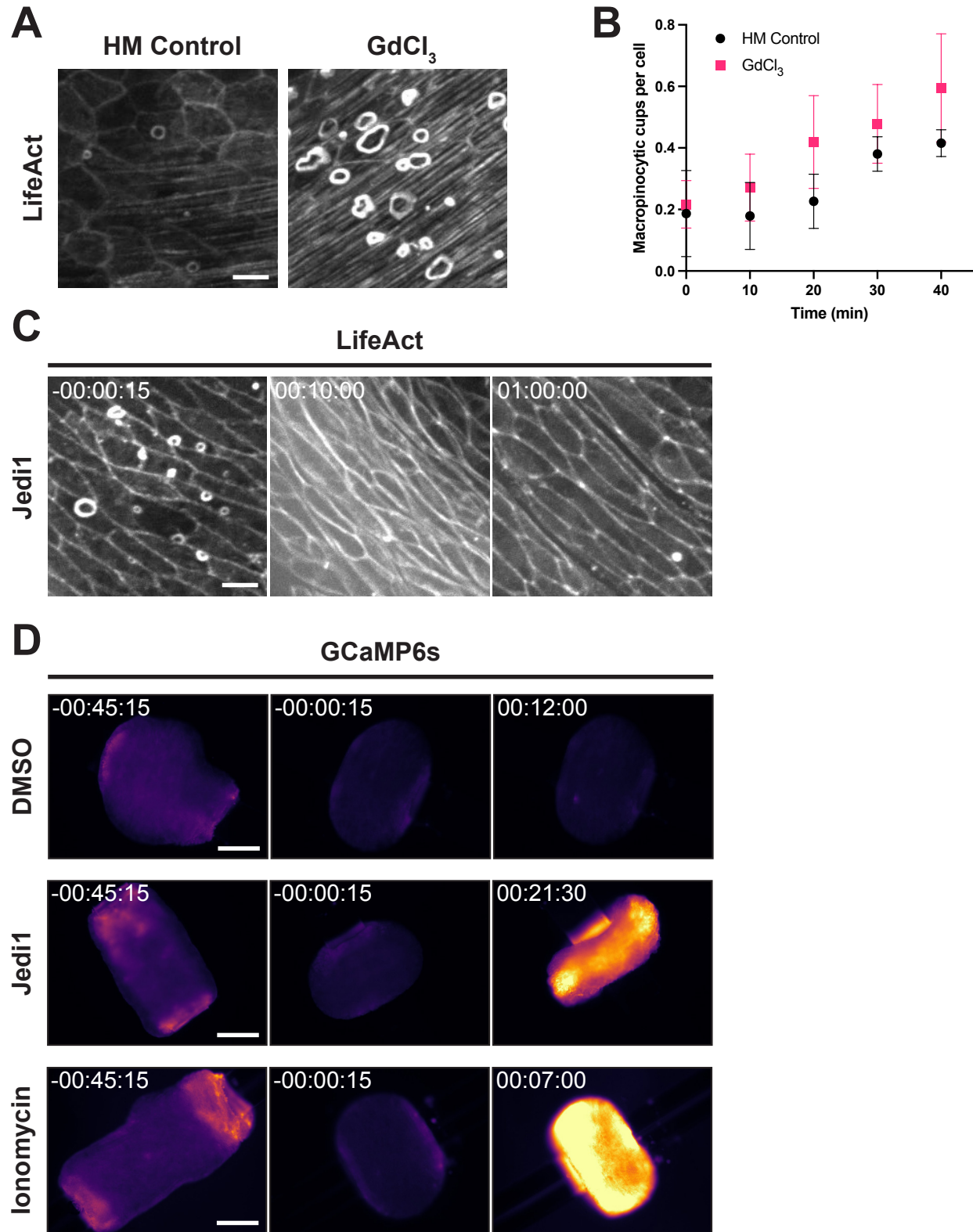


**Figure S3.2.** A) Representative images of live, intact *Hydra* expressing LifeAct-GFP in the ectoderm, treated with control *Hydra* medium (left) or GdCl<sub>3</sub> (right; 50  $\mu$ M for 15 min). B)

Quantification of macropinocytic cup frequency in *Hydra* medium control (black) and GdCl<sub>3</sub>-treated (magenta; 50 μM) threaded body columns over time (mean ± sd; n = 4 independent sample preparations per condition). Note that HM control data is duplicated from **Fig. 3.2A**. C) Representative time-course of a threaded body column expressing LifeAct-GFP in the ectoderm before (left) and after (center, right) treatment with Jedi1 (200 μM). (A, C) Scale bars, 20 μm. All frames depict maximum intensity projections of 15–35 μm z-stacks. D) Representative time-courses of threaded body columns expressing GCaMP6s in the ectoderm, before (left, center) and after (right) DMSO, Jedi1 (200 μM), or Ionomycin (10 μM) treatment. Images depict single z-sections. Scale bars, 500 μm. (C, D) Time stamps indicate time relative to drug addition; hh:mm:ss.

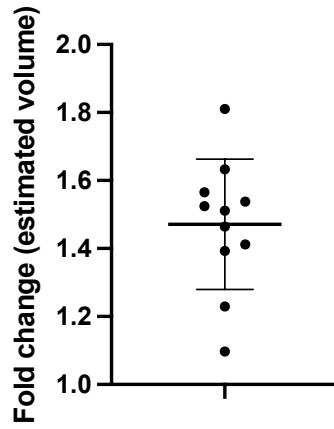


**Figure S3.3.** Quantification of the approximated fold change in spheroid volume achievable prior to tissue rupture during spheroid inflation (bars: mean  $\pm$  sd; n = 11 from 4 independent sample preparations).

## Materials and methods

### *Hydra culturing and strains*

*Hydra* were maintained at 18 °C in *Hydra* medium and fed 2-3 times per week with *Artemia* nauplii (Brine Shrimp Direct). Animals were starved  $\geq$  24h prior to experimentation, and non-budding animals were chosen for experimentation. The following transgenic lines were used:

DsRed2(ectoderm)/GFP(endoderm) [59]

LifeAct-GFP(ectoderm) [47]

pActin::GCaMP6s(ectoderm) [90]

AEP SS1 (courtesy of Rob Steele)

### *Microscopy*

Immunofluorescence and live images of LifeAct-expressing spheroids and body columns were acquired on a Yokogawa CSU100 spinning disk confocal attached to an inverted Nikon Ti-E microscope, with Hamamatsu C9100-13 EMCCD camera, using 20X Plan Apo VC 0.75 NA or 60XA Plan Apo VC 1.20 NA WI objectives. Images of GCaMP6s-expressing spheroids were acquired on an inverted Nikon Ti-E microscope with Lumencor SpectraX epifluorescence module and Andor Zyla camera, using a 10X Plan Apo 0.45 NA objective. Images of GCaMP6s-expressing body columns were acquired on an inverted Zeiss Axiovert 200M microscope with and Point Grey Chamelion3 Monochrome camera, using a 5X EC Plan-Neofluar 0.16 NA objective. Confocal Z-stacks were acquired at 2-10  $\mu$ m step sizes for a total depth of 30-100  $\mu$ m, at 4-60 s time intervals. Where epifluorescence was used, images were acquired at a fixed focal plane at 5-30 s intervals. All images were acquired using Micro-Manager software [65].



### *Immunofluorescence*

Immunofluorescence was performed as previously described [47], with slight modification. In brief, AEP SS1 *Hydra* were relaxed for 1 min in 2% urethane (Sigma, Cat# 51-79-6)/*Hydra* medium, fixed for 1 h in 4% PFA (Electron Microscopy Sciences, Cat# 15714)/*Hydra* medium, washed 3x in PBS (Gibco, Cat# 20012-027), permeabilized for 15 min in 0.5% Triton X-100 (Sigma, Cat# 9036-19-5)/PBS, blocked for 1 h in 1% BSA (Sigma, Cat# A7906)/0.1% Triton X-100/PBS (blocking solution), stained for 1 h in Alexa 488-phalloidin (Invitrogen, Cat# A12379) diluted to 1:200 in blocking solution, washed 3x in PBS, and mounted between a glass slide and coverslip with ProLong Gold mounting medium (Invitrogen, Cat# P36930).

### *Tissue manipulations*

Threaded body columns were prepared by amputating the head and foot (peduncle) from *Hydra* with a scalpel and inserting a 5-10 mm length of 8-lb fishing line (Trilene SensiThin) through the exposed lumen. Body columns were allowed to stabilize for 15 min prior to chemical perturbations, but were otherwise imaged immediately after preparation and transfer to imaging vessels, which consisted of either 35mm glass bottom dishes (MatTek, P35G-1.5-14-C) or 96-well glass bottom plates (MatriPlate, MGB096-1-2-LG-L).

Spheroids were prepared by removing the head and foot from *Hydra* and cutting the remaining body column into 3-4 rings, which were subsequently cut longitudinally into 2-3 sections. Dissected tissues were allowed to heal unperturbed for 12-24 h prior to experimentation. Micro-injection/inflation was achieved using a micropipette mounted to a Narishige motor-driven micro-manipulator (MM-94) via Narishige microscope mounting adaptor, injection holder, and universal joint (NN-H-4, HI-9, UT-2, respectively). Pipettes were pulled from Sutter Instrument

capillary tubes (#B150-110-10) on a Sutter Instrument micropipette puller (P-1000). Fluid ejection was controlled by a syringe attached to the pipette. Inflations were performed over a period of 2-3 minutes, after which the micropipette was immediately removed. Only spheroids that remained intact (did not rupture) were used to quantify macropinocytic cup abundance/dynamics. For mock inflations, a micropipette was inserted into the spheroid for 3 minutes, without injection, before removal.

#### *Dextran uptake*

Macropinosomes and dextran uptake were visualized by transferring stabilized threaded body columns to a solution containing pHrodo Red Dextran, 10,000 MW (ThermoFisher, Cat# P10361) diluted to 5  $\mu\text{g}/\text{mL}$  in *Hydra* medium, and immediately beginning acquisitions.

#### *Chemical perturbations*

$\text{GdCl}_3$  (Sigma, Cat# 439770) stock solution was prepared in *Hydra* medium and diluted to a final concentration of 50  $\mu\text{M}$ . For immunofluorescence experiments, animals were directly transferred to either the 50  $\mu\text{M}$   $\text{GdCl}_3$  solution or fresh *Hydra* medium (HM control) and incubated for 15 min prior to fixation. For threaded body column experiments,  $\text{GdCl}_3$  was diluted directly into imaging chamber *Hydra* medium to a final concentration of 50  $\mu\text{M}$ . For drug perturbations, Jedi1 (Sigma, SML2533), Jedi2 (Sigma, SML2532), and ionomycin calcium salt (Sigma, I0634) stock solutions were prepared in DMSO and diluted directly into imaging chamber *Hydra* medium to final concentrations of 200  $\mu\text{M}$ , 200  $\mu\text{M}$ , and 10  $\mu\text{M}$ , respectively. DMSO controls corresponded to the highest DMSO concentration (1% v/v) present in drug treatments.

### *Quantification and Statistical Analysis*

Measurements of macropinocytic cup sizes were performed in FIJI using the built-in measure function for a line segment drawn along the long axis of macropinocytic cups at their maximum width. Measures of macropinocytic cups per cell were obtained from manual counts of macropinocytic cups and cells occupying the microscope field of view at a given time point. Quantifications assigned to the head, body column, and foot were generated from images obtained from the top, middle, and bottom 1/3 of the animal's body length (tentacles excluded). Quantification of macropinosomes was similarly obtained by manual counts of dextran-filled puncta at a given time point. Average GCaMP6s fluorescence intensity was quantified by generating binary masks corresponding to body columns or spheroids in each frame, applying masks to unadulterated images to define regions of interest (ROIs), and quantifying the mean gray value of all pixels within the specified ROI using FIJI's built-in measure function. The estimated fold change in spheroid volume before rupture was determined by approximating each spheroid as a true sphere and using the manually measured radius along the spheroid long axis before and after inflation (until rupture) for calculations.

### **Acknowledgments**

We thank Celina Juliano and Rob Steele for numerous insights into *Hydra* care and experimentation. We are grateful to Rob Steele and Rafael Yuste for providing additional *Hydra* lines and reagents. This material is based upon work supported by the National Science Foundation Graduate Research Fellowship under Grant No. 1650113 (to TDS). TDS was also supported by the UCSF Chuan Lyu Discovery Fellowship. BH was supported by the Marie Skłodowska-Curie COFUND program ARDRE “Ageing, Regeneration and Drug Research” (Grant No. 847681).

KLM was supported by the Damon Runyon Cancer Research Foundation (DRG-2282-17 and DFS-47-21) and by the Eunice Kennedy Shriver National Institute Of Child Health & Human Development of the National Institutes of Health (K99HD101021). RDV was supported by the Howard Hughes Medical Institute.

## CHAPTER 4

### Final Thoughts

The studies described herein illustrate mechanisms by which cells can be coordinated to drive complex emergent behaviors and properties in tissues and organs. These examples, though disparate in nature and representing only a fraction of the complexity of physiological phenomena, collectively reveal the importance of cellular coordination in both the formation and function of tissues.

Our findings regarding cell sorting in *Hydra*, especially that epithelialized ectodermal collectives are capable of internalizing cells derived from all lineages, highlight an important, yet often overlooked, feature of aggregate regeneration: the mechanisms of cell sorting in *Hydra* are prone to error. This has been well described in prior work illustrating the regenerative process over extended time frames, revealing that aggregates routinely generate defects consisting of internalized ectodermal compartments, which gradually resolve over subsequent days [46]. It is conceivable that these mis-localized ectodermal compartments result from the stochastic internalization of ectodermal cells by the reforming epithelium, paralleling the ectodermal internalization induced in our study.

This observation is important for two reasons. First, it suggests that a vital component of aggregate patterning, including at the tissue scale, occurs downstream of the initial events widely regarded as “sorting,” with the resolution of patterning defects. How these defects are resolved remains an open question, and one that will require close attention to stages of regeneration often ignored by those interested in cell sorting. Considerable cell death and elimination occurs during aggregate regeneration [25]. While this undoubtedly accounts for the resolution of some sorting

errors, whether cells are biased toward elimination based on their positioning, either through necrosis or programmed cell death, is unknown. Similarly, it remains unknown whether mis-localized cells can reintegrate into functional tissues. Given the error-prone mechanism of sorting we describe and the prevalence of patterning defects in aggregates, rationalizing how these defects are resolved represents an important step toward a complete understanding of tissue patterning in *Hydra*.

Second, the error-prone nature of cell sorting raises the possibility that high-fidelity tissue patterning may not be the outcome for which the underlying mechanisms evolved. *Hydra* is unlikely to experience, let alone survive, the degree of catastrophic tissue damage associated with experimental reaggregation in nature, rendering it an unlikely selective pressure. Moreover, our findings reveal striking similarities in the cell behaviors associated with cell sorting and local wound closure in *Hydra*, suggesting that similar mechanisms may underly these processes. Consequently, we speculate that the mechanisms in question may have evolved to promote rapid wound healing, particularly epithelial restoration and barrier formation, and that the efficient execution of these processes across large length scales may be sufficient to account for the early stages of tissue repatterning in *Hydra*. Although we cannot exclude the possibility that cell sorting instead reflects an elaboration of developmental programs required for embryonic patterning, as has been suggested in other model systems [7], we believe that such a justification is not necessary, nor currently scientifically supported, in *Hydra*. Future molecular dissection of the mechanisms underlying cell sorting, wound healing, and embryonic patterning in *Hydra* may shed light on the evolutionary origins of this phenomenon.

Importantly, our work on this matter does not refute prior findings suggesting a role for differential interfacial tension in *Hydra* cell sorting [26,27], nor are the proposed models mutually

exclusive. Instead, we perceive our findings as complimentary in that they not only reveal cell behaviors potentially contributing to reported differences in tissue surface tension, but also contributions that may be overlooked by these thermodynamically centered models. This is especially true for behaviors or properties that may influence the survival of aggregates as regeneration unfolds, such as osmotic barrier restoration, which may result in local deviations in the biophysical properties of tissues that are not accounted for in these models. Similarly, this notion applies to those cellular behaviors that might influence the rate of cell mixing within aggregates, effectively determining the kinetics of already energetically favorable sorting outcomes.

In contrast to the role for cellular coordination in tissue assembly, Chapter 3 of this thesis deals with the coordination of cells in already assembled tissues. Here, these principles are no less important, as *Hydra* relies on the coordination of cells to orient and synchronize a number of processes required for homeostasis and regeneration [34,36,37]. In this work, we detail the discovery of constitutive macropinocytosis in the *Hydra* ectodermal epithelium and highlight a role for cellular stretch in regulating this process.

The effect of tissue mechanics in regulating fluid uptake and membrane recycling in *Hydra* has potentially important implications for *Hydra*'s physiology. We note that the high rates of macropinocytosis we observed, especially in isolated body columns, can account for considerable membrane retrieval. We observed no apparent reductions in apical cell surface area to suggest that membrane retrieval outpaced membrane deposition. This suggests that membrane recycling in *Hydra* is likely tightly regulated. While speculative, if and how this coupling may be regulated to maintain homeostatic tension in the animal's body column presents an interesting direction for

future studies. Given *Hydra*'s highly elastic body, it is conceivable that this mode of membrane retrieval may contribute to the cellular rearrangements observed during development [107].

Our work on macropinocytosis in *Hydra* highlights an example of constitutive fluid engulfment occurring in epithelial tissues, contrasting most forms of constitutive macropinocytosis attributed to specialized cell types [94]. Thus, further dissection of this phenomenon may ultimately reveal novel functions of a well-characterized biological process. Given the amenability of *Hydra* to live imaging and experimental manipulation, this system provides a useful tool for the mechanistic dissection of constitutive macropinocytosis and its associated actin remodeling in physiological contexts.

Together, these studies illustrate how meaningful insights into well-characterized biological processes can be gained from the exploration of phenomena in understudied systems, and how these systems may be chosen with an eye toward the development of effective approaches to visualize and manipulate them in physiological contexts. *Hydra*'s unique features—a relatively simple anatomy, broad regenerative potential, and wealth of unexplored cell biology—make it an obvious candidate for these purposes; however, the steady emergence of new molecular genetic tools, culturing capabilities, and imaging modalities promises to bring unforeseen numbers of experimental systems within reach. It is the hope that in this space, where cellular, organismal, and habitat diversity may be sufficiently sampled, the true diversity of biological phenomena and their underlying mechanisms may finally begin to be uncovered.



## REFERENCES

1. Garcia, M.A., Nelson, W.J., and Chavez, N. (2018). Cell–Cell Junctions Organize Structural and Signaling Networks. *Cold Spring Harb Perspect Biol* *10*, a029181.
2. Lecuit, T., Lenne, P.-F., and Munro, E. (2011). Force Generation, Transmission, and Integration during Cell and Tissue Morphogenesis. *Annu. Rev. Cell Dev. Biol.* *27*, 157–184.
3. Deneke, V.E., and Di Talia, S. (2018). Chemical waves in cell and developmental biology. *Journal of Cell Biology* *217*, 1193–1204.
4. Browne, E.N. (1909). The production of new hydranths in Hydra by the insertion of small grafts. *J. Exp. Zool.* *7*, 1–23.
5. Morgan, T.H. (1901). *Regeneration* (Macmillan).
6. Spemann, H., and Mangold, H. (1924). über Induktion von Embryonalanlagen durch Implantation artfremder Organisatoren. *Archiv f mikr Anat u Entwicklungsmechanik* *100*, 599–638.
7. Townes, P., and Holtfreter, J. (1955). Directed movements and selective adhesion of embryonic amphibian cells. *Journal of Experimental Zoology* *128*, 53–120.
8. Steinberg, M.S. (1962). On the mechanism of tissue reconstruction by dissociated cells, I. Population kinetics, differential adhesiveness, and the absence of directed migration. *Proc Natl Acad Sci U S A* *48*, 1577–1582.
9. Phillips, H.M., and Steinberg, M.S. (1969). Equilibrium Measurements of Embryonic Chick Cell Adhesiveness, I. Shape Equilibrium in Centrifugal Fields. *PNAS* *64*, 121–127.

10. Duguay, D., Foty, R.A., and Steinberg, M.S. (2003). Cadherin-mediated cell adhesion and tissue segregation: qualitative and quantitative determinants. *Developmental Biology* 253, 309–323.
11. Foty, R.A., and Steinberg, M.S. (2005). The differential adhesion hypothesis: a direct evaluation. *Developmental Biology* 278, 255–263.
12. Steinberg, M.S., and Takeichi, M. (1994). Experimental specification of cell sorting, tissue spreading, and specific spatial patterning by quantitative differences in cadherin expression. *PNAS* 91, 206–209.
13. Steinberg, M.S. (1970). Does differential adhesion govern self-assembly processes in histogenesis? Equilibrium configurations and the emergence of a hierarchy among populations of embryonic cells. *Journal of Experimental Zoology* 173, 395–433.
14. Brodland, G.W., and Chen, H.H. (2000). The Mechanics of Heterotypic Cell Aggregates: Insights From Computer Simulations. *J Biomech Eng* 122, 402–407.
15. Brodland, G.W. (2002). The Differential Interfacial Tension Hypothesis (DITH): A Comprehensive Theory for the Self-Rearrangement of Embryonic Cells and Tissues. *J Biomech Eng* 124, 188–197.
16. Foty, R.A., and Steinberg, M.S. (2013). Differential adhesion in model systems. *Wiley Interdisciplinary Reviews: Developmental Biology* 2, 631–645.
17. Ninomiya, H., David, R., Damm, E.W., Fagotto, F., Niessen, C.M., and Winklbauer, R. (2012). Cadherin-dependent differential cell adhesion in *Xenopus* causes cell sorting in vitro but not in the embryo. *J Cell Sci* 125, 1877–1883.
18. Krens, S.F.G., Veldhuis, J.H., Barone, V., Čapek, D., Maître, J.-L., Brodland, G.W., and Heisenberg, C.-P. (2017). Interstitial fluid osmolarity modulates the action of differential

- tissue surface tension in progenitor cell segregation during gastrulation. *Development* *144*, 1798–1806.
19. Schötz, E.-M., Burdine, R.D., Jülicher, F., Steinberg, M.S., Heisenberg, C.-P., and Foty, R.A. (2008). Quantitative differences in tissue surface tension influence zebrafish germ layer positioning. *HFSP Journal* *2*, 42–56.
  20. Lancaster, M.A., and Knoblich, J.A. (2014). Organogenesis in a dish: Modeling development and disease using organoid technologies. *Science* *345*.
  21. Simunovic, M., and Brivanlou, A.H. (2017). Embryoids, organoids and gastruloids: new approaches to understanding embryogenesis. *Development* *144*, 976–985.
  22. Technau, U., and Steele, R.E. (2011). Evolutionary crossroads in developmental biology: Cnidaria. *Development* *138*, 1447–1458.
  23. Wittlieb, J., Khalturin, K., Lohmann, J.U., Anton-Erxleben, F., and Bosch, T.C.G. (2006). Transgenic Hydra allow in vivo tracking of individual stem cells during morphogenesis. *Proceedings of the National Academy of Sciences* *103*, 6208–6211.
  24. Trembley, A. (1744). Mémoires, pour servir à l’histoire d’un genre de polypes d’eau douce, à bras en forme de cornes (Chez Jean & Herman Verbeek).
  25. Gierer, A., Berking, S., Bode, H., David, C.N., Flick, K., Hansmann, G., Schaller, H., and Trenkner, E. (1972). Regeneration of Hydra from Reaggregated Cells. *Nature New Biology* *239*, 98–101.
  26. Technau, U., and Holstein, T.W. (1992). Cell sorting during the regeneration of Hydra from reaggregated cells. *Developmental Biology* *151*, 117–127.
  27. Cochet-Escartin, O., Locke, T.T., Shi, W.H., Steele, R.E., and Collins, E.-M.S. (2017). Physical Mechanisms Driving Cell Sorting in Hydra. *Biophysical Journal* *113*, 2827–2841.

28. Sato-Maeda, M., Uchida, M., Graner, F., and Tashiro, H. (1994). Quantitative Evaluation of Tissue-Specific Cell Adhesion at the Level of a Single Cell Pair. *Developmental Biology* *162*, 77–84.
29. Kishimoto, Y., Murate, M., and Sugiyama, T. (1996). Hydra regeneration from recombined ectodermal and endodermal tissue. I. Epibolic ectodermal spreading is driven by cell intercalation. *Journal of Cell Science* *109*, 763–772.
30. Takaku, Y., Hariyama, T., and Fujisawa, T. (2005). Motility of endodermal epithelial cells plays a major role in reorganizing the two epithelial layers in Hydra. *Mechanisms of Development* *122*, 109–122.
31. Rieu, J.P., Kataoka, N., and Sawada, Y. (1998). Quantitative analysis of cell motion during sorting in two-dimensional aggregates of dissociated hydra cells. *Physical Review E* *57*, 924–931.
32. Rieu, J.P., Upadhyaya, A., Glazier, J.A., Ouchi, N.B., and Sawada, Y. (2000). Diffusion and Deformations of Single Hydra Cells in Cellular Aggregates. *Biophysical Journal* *79*, 1903–1914.
33. Hand, A.R., and Gobel, S. (1972). The structural organization of the septate and gap junctions of Hydra. *Journal of Cell Biology* *52*, 397–408.
34. Fraser, S.E., Green, C.R., Bode, H.R., and Gilula, N.B. (1987). Selective disruption of gap junctional communication interferes with a patterning process in Hydra. *Science* *237*, 49–55.
35. Wood, R.L. (1979). The fine structure of the hypostome and mouth of hydra. *Cell Tissue Res.* *199*, 319–338.

36. Shimizu, H., Bode, P.M., and Bode, H.R. (1995). Patterns of oriented cell division during the steady-state morphogenesis of the body column in hydra. *Developmental Dynamics* 204, 349–357.
37. Beitch, B.R. (1968). The contractile system of hydra, as studied with saponin-extracted models and electron microscopy. Available at:  
[https://libraetd.lib.virginia.edu/public\\_view/5138jff19t](https://libraetd.lib.virginia.edu/public_view/5138jff19t) [Accessed December 27, 2021].
38. Krens, S.F.G., and Heisenberg, C.-P. (2011). Cell Sorting in Development. In *Current Topics in Developmental Biology* (Elsevier), pp. 189–213.
39. Foty, R.A., Pflieger, C.M., Forgacs, G., and Steinberg, M.S. (1996). Surface tensions of embryonic tissues predict their mutual envelopment behavior. *Development* 122, 1611–1620.
40. Steinberg, M.S. (1962). On the Mechanism of Tissue Reconstruction by Dissociated Cells, III. Free Energy Relations and the Reorganization of Fused, Heteronomic Tissue Fragments. *PNAS* 48, 1769–1776.
41. Fagotto, F., Rohani, N., Touret, A.-S., and Li, R. (2013). A Molecular Base for Cell Sorting at Embryonic Boundaries: Contact Inhibition of Cadherin Adhesion by Ephrin/Eph-Dependent Contractility. *Developmental Cell* 27, 72–87.
42. Landsberg, K.P., Farhadifar, R., Ranft, J., Umetsu, D., Widmann, T.J., Bittig, T., Said, A., Jülicher, F., and Dahmann, C. (2009). Increased Cell Bond Tension Governs Cell Sorting at the *Drosophila* Anteroposterior Compartment Boundary. *Current Biology* 19, 1950–1955.
43. Monier, B., Pélissier-Monier, A., Brand, A.H., and Sanson, B. (2010). An actomyosin-based barrier inhibits cell mixing at compartmental boundaries in *Drosophila* embryos. *Nature Cell Biology* 12, 60–65.

44. Hobmayer, B., Snyder, P., Alt, D., Happel, C.M., and Holstein, T.W. (2001). Quantitative analysis of epithelial cell aggregation in the simple metazoan Hydra reveals a switch from homotypic to heterotypic cell interactions. *Cell Tissue Res* 304, 147–157.
45. Takaku, Y., Hariyama, T., Kurachi, M., and Tsukahara, Y. (1999). Ultrastructural observations of adherent cell pairs in hydra vulgaris. *Journal of Experimental Biology* 202, 2239–2244.
46. Seybold, A., Salvenmoser, W., and Hobmayer, B. (2016). Sequential development of apical-basal and planar polarities in aggregating epitheliomuscular cells of Hydra. *Developmental Biology* 412, 148–159.
47. Aufschnaiter, R., Wedlich-Söldner, R., Zhang, X., and Hobmayer, B. (2017). Apical and basal epitheliomuscular F-actin dynamics during Hydra bud evagination. *Biol Open* 6, 1137–1148.
48. Holz, O., Apel, D., Steinmetz, P., Lange, E., Hopfenmüller, S., Ohler, K., Sudhop, S., and Hassel, M. (2017). Bud detachment in hydra requires activation of fibroblast growth factor receptor and a Rho–ROCK–myosin II signaling pathway to ensure formation of a basal constriction. *Developmental Dynamics* 246, 502–516.
49. Vicente-Manzanares, M., Ma, X., Adelstein, R.S., and Horwitz, A.R. (2009). Non-muscle myosin II takes centre stage in cell adhesion and migration. *Nat Rev Mol Cell Biol* 10, 778–790.
50. Courtemanche, N., Pollard, T.D., and Chen, Q. (2016). Avoiding artefacts when counting polymerized actin in live cells with LifeAct fused to fluorescent proteins. *Nature Cell Biology* 18, 676–683.

51. Flores, L.R., Keeling, M.C., Zhang, X., Sliogeryte, K., and Gavara, N. (2019). Lifeact-TagGFP2 alters F-actin organization, cellular morphology and biophysical behaviour. *Scientific Reports* 9, 3241.
52. Paluch, E., Piel, M., Prost, J., Bornens, M., and Sykes, C. (2005). Cortical Actomyosin Breakage Triggers Shape Oscillations in Cells and Cell Fragments. *Biophysical Journal* 89, 724–733.
53. Bement, W.M., Forscher, P., and Mooseker, M.S. (1993). A novel cytoskeletal structure involved in purse string wound closure and cell polarity maintenance. *J. Cell Biol.* 121, 565–578.
54. Nusrat, A., Delp, C., and Madara, J.L. (1992). Intestinal epithelial restitution. Characterization of a cell culture model and mapping of cytoskeletal elements in migrating cells. *J Clin Invest* 89, 1501–1511.
55. Luu, O., David, R., Ninomiya, H., and Winklbauer, R. (2011). Large-scale mechanical properties of *Xenopus* embryonic epithelium. *PNAS* 108, 4000–4005.
56. Holtfreter, J. (1944). A study of the mechanics of gastrulation. Part II. *Journal of Experimental Zoology* 95, 171–212.
57. Holtfreter, J. (1943). Properties and functions of the surface coat in amphibian embryos. *Journal of Experimental Zoology* 93, 251–323.
58. Sarras, M.P., Zhang, X., Huff, J.K., Accavitti, M.A., St. John, P.L., and Abrahamson, D.R. (1993). Extracellular Matrix (Mesoglea) of *Hydra vulgaris*: III. Formation and Function during Morphogenesis of *Hydra* Cell Aggregates. *Developmental Biology* 157, 383–398.

59. Glauber, K.M., Dana, C.E., Park, S.S., Colby, D.A., Noro, Y., Fujisawa, T., Chamberlin, A.R., and Steele, R.E. (2013). A small molecule screen identifies a novel compound that induces a homeotic transformation in Hydra. *Development* *140*, 4788–4796.
60. Hemmrich, G., Khalturin, K., Boehm, A.-M., Puchert, M., Anton-Erxleben, F., Wittlieb, J., Klostermeier, U.C., Rosenstiel, P., Oberg, H.-H., Domazet-Lošo, T., *et al.* (2012). Molecular Signatures of the Three Stem Cell Lineages in Hydra and the Emergence of Stem Cell Function at the Base of Multicellularity. *Mol Biol Evol* *29*, 3267–3280.
61. Siebert, S., Farrell, J.A., Cazet, J.F., Abeykoon, Y., Primack, A.S., Schnitzler, C.E., and Juliano, C.E. (2019). Stem cell differentiation trajectories in Hydra resolved at single-cell resolution. *Science* *365*, eaav9314.
62. Juliano, C.E., Lin, H., and Steele, R.E. (2014). Generation of Transgenic Hydra by Embryo Microinjection. *J Vis Exp*.
63. The UniProt Consortium (2019). UniProt: a worldwide hub of protein knowledge. *Nucleic Acids Res* *47*, D506–D515.
64. Lenhoff, H. (2013). *Hydra: Research Methods* (Springer Science & Business Media).
65. Edelstein, A., Amodaj, N., Hoover, K., Vale, R., and Stuurman, N. (2010). Computer control of microscopes using  $\mu$ Manager. *Current Protocols in Molecular Biology* *92*, 14.20.1-14.20.17.
66. Kerr, M.C., and Teasdale, R.D. (2009). Defining macropinocytosis. *Traffic* *10*, 364–371.
67. Bloomfield, G., and Kay, R.R. (2016). Uses and abuses of macropinocytosis. *Journal of Cell Science* *129*, 2697–2705.



68. Bloomfield, G., Traynor, D., Sander, S.P., Veltman, D.M., Pachebat, J.A., and Kay, R.R. (2015). Neurofibromin controls macropinocytosis and phagocytosis in *Dictyostelium*. *eLife* 4, e04940.
69. Commisso, C., Davidson, S.M., Soydaner-Azeloglu, R.G., Parker, S.J., Kamphorst, J.J., Hackett, S., Grabocka, E., Nofal, M., Drebin, J.A., Thompson, C.B., *et al.* (2013). Macropinocytosis of protein is an amino acid supply route in Ras-transformed cells. *Nature* 497, 633–637.
70. Sallusto, F., Cella, M., Danieli, C., and Lanzavecchia, A. (1995). Dendritic cells use macropinocytosis and the mannose receptor to concentrate macromolecules in the major histocompatibility complex class II compartment: Downregulation by cytokines and bacterial products. *Journal of Experimental Medicine* 182, 389–400.
71. Sarkar, K., Kruhlak, M.J., Erlandsen, S.L., and Shaw, S. (2005). Selective inhibition by rottlerin of macropinocytosis in monocyte-derived dendritic cells. *Immunology* 116, 513–524.
72. Orth, J.D., Krueger, E.W., Weller, S.G., and McNiven, M.A. (2006). A novel endocytic mechanism of epidermal growth factor receptor sequestration and internalization. *Cancer Res* 66, 3603–3610.
73. Clayton, E.L., Evans, G.J.O., and Cousin, M.A. (2008). Bulk synaptic vesicle endocytosis is rapidly triggered during strong stimulation. *J. Neurosci.* 28, 6627–6632.
74. Holt, M., Cooke, A., Wu, M.M., and Lagnado, L. (2003). Bulk membrane retrieval in the synaptic terminal of retinal bipolar cells. *J Neurosci* 23, 1329–1339.
75. Buckley, C.M., and King, J.S. (2017). Drinking problems: Mechanisms of macropinosome formation and maturation. *The FEBS Journal* 284, 3778–3790.

76. Rosales-Reyes, R., Pérez-López, A., Sánchez-Gómez, C., Hernández-Mote, R.R., Castro-Eguiluz, D., Ortiz-Navarrete, V., and Alpuche-Aranda, C.M. (2012). Salmonella infects B cells by macropinocytosis and formation of spacious phagosomes but does not induce pyroptosis in favor of its survival. *Microbial Pathogenesis* 52, 367–374.
77. West, M.A., Bretscher, M.S., and Watts, C. (1989). Distinct endocytotic pathways in epidermal growth factor-stimulated human carcinoma A431 cells. *Journal of Cell Biology* 109, 2731–2739.
78. Chiasson-MacKenzie, C., Morris, Z.S., Liu, C.-H., Bradford, W.B., Koorman, T., and McClatchey, A.I. (2018). Merlin/ERM proteins regulate growth factor-induced macropinocytosis and receptor recycling by organizing the plasma membrane:cytoskeleton interface. *Genes Dev.* Available at: <http://genesdev.cshlp.org/content/early/2018/08/24/gad.317354.118> [Accessed September 3, 2018].
79. Lin, S.-S., and Liu, Y.-W. (2019). Mechanical stretch induces mTOR recruitment and activation at the phosphatidic acid-enriched macropinosome in muscle cell. *Front Cell Dev Biol* 7. Available at: <https://www.ncbi.nlm.nih.gov/pmc/articles/PMC6518962/> [Accessed June 10, 2021].
80. Loh, J., Chuang, M.-C., Lin, S.-S., Joseph, J., Su, Y.-A., Hsieh, T.-L., Chang, Y.-C., Liu, A.P., and Liu, Y.-W. (2019). An acute decrease in plasma membrane tension induces macropinocytosis via PLD2 activation. *Journal of Cell Science* 132. Available at: <https://doi.org/10.1242/jcs.232579> [Accessed May 28, 2021].
81. Lin, X.P., Mintern, J.D., and Gleeson, P.A. (2020). Macropinocytosis in different cell types: Similarities and differences. *Membranes* 10, 177.

82. Skokan, T.D., Vale, R.D., and McKinley, K.L. (2020). Cell sorting in *Hydra vulgaris* arises from differing capacities for epithelialization between cell types. *Current Biology* 30, 3713-3723.e3.
83. Beams, H.W., Kessel, R.G., and Shih, C.-Y. (1973). The surface features of *Hydra* as revealed by scanning electron microscopy. *Transactions of the American Microscopical Society* 92, 161.
84. Mellström, K., Höglund, A.-S., Nistér, M., Heldin, C.-H., Westermark, B., and Lindberg, U. (1983). The effect of platelet-derived growth factor on morphology and motility of human glial cells. *J Muscle Res Cell Motil* 4, 589–609.
85. Buccione, R., Orth, J.D., and McNiven, M.A. (2004). Foot and mouth: Podosomes, invadopodia and circular dorsal ruffles. *Nature Reviews Molecular Cell Biology* 5, 647–657.
86. Stewart, T.A., and Davis, F.M. (2019). Formation and function of mammalian epithelia: Roles for mechanosensitive PIEZO1 ion channels. *Frontiers in Cell and Developmental Biology* 7, 260.
87. Yang, X., and Sachs, F. (1989). Block of stretch-activated ion channels in *Xenopus* oocytes by gadolinium and calcium ions. *Science* 243, 1068–1071.
88. Wang, Y., Chi, S., Guo, H., Li, G., Wang, L., Zhao, Q., Rao, Y., Zu, L., He, W., and Xiao, B. (2018). A lever-like transduction pathway for long-distance chemical- and mechano-gating of the mechanosensitive Piezo1 channel. *Nat Commun* 9, 1300.
89. Coste, B., Mathur, J., Schmidt, M., Earley, T.J., Ranade, S., Petrus, M.J., Dubin, A.E., and Patapoutian, A. (2010). Piezo1 and Piezo2 are essential components of distinct mechanically activated cation channels. *Science* 330, 55–60.

90. Szymanski, J.R., and Yuste, R. (2019). Mapping the whole-body muscle activity of *Hydra vulgaris*. *Current Biology* 29, 1807-1817.e3.
91. Sato-Maeda, M., and Tashiro, H. (1999). Development of oriented motion in regenerating *Hydra* cell aggregates. *J. exp. Zool.* 16, 327–334.
92. Shimizu, H., Sawada, Y., and Sugiyama, T. (1993). Minimum tissue size required for *Hydra* regeneration. *Developmental Biology* 155, 287–296.
93. King, J.S., and Kay, R.R. (2019). The origins and evolution of macropinocytosis. *Philosophical Transactions of the Royal Society B: Biological Sciences* 374, 20180158.
94. Liu, Z., and Roche, P.A. (2015). Macropinocytosis in phagocytes: Regulation of MHC class-II-restricted antigen presentation in dendritic cells. *Frontiers in Physiology* 6, 1.
95. Ganot, P., Tambutté, E., Caminiti-Segonds, N., Toullec, G., Allemand, D., and Tambutté, S. (2020). Ubiquitous macropinocytosis in anthozoans. *eLife* 9, e50022.
96. Diz-Muñoz, A., Thurley, K., Chintamen, S., Altschuler, S.J., Wu, L.F., Fletcher, D.A., and Weiner, O.D. (2016). Membrane tension acts through PLD2 and mTORC2 to limit actin network assembly during neutrophil migration. *PLOS Biology* 14, e1002474.
97. Houk, A.R., Jilkine, A., Mejean, C.O., Boltyanskiy, R., Dufresne, E.R., Angenent, S.B., Altschuler, S.J., Wu, L.F., and Weiner, O.D. (2012). Membrane tension maintains cell polarity by confining signals to the leading edge during neutrophil migration. *Cell* 148, 175–188.
98. Aghamohammadzadeh, S., and Ayscough, K.R. (2009). Under pressure: The differential requirements for actin during yeast and mammalian endocytosis. *Nat Cell Biol* 11, 1039–1042.

99. Eisenhoffer, G.T., Loftus, P.D., Yoshigi, M., Otsuna, H., Chien, C.-B., Morcos, P.A., and Rosenblatt, J. (2012). Crowding induces live cell extrusion to maintain homeostatic cell numbers in epithelia. *Nature* 484, 546–549.
100. Gudipaty, S.A., Lindblom, J., Loftus, P.D., Redd, M.J., Edes, K., Davey, C.F., Krishnegowda, V., and Rosenblatt, J. (2017). Mechanical stretch triggers rapid epithelial cell division through Piezo1. *Nature* 543, 118–121.
101. Kuriyama, M., Hirose, H., Masuda, T., Shudou, M., Arafles, J.V.V., Imanishi, M., Maekawa, M., Hara, Y., and Futaki, S. (2021). Piezo1 activation using Yoda1 inhibits macropinocytosis and proliferation of cancer cells. *bioRxiv*, 2021.05.14.444123.
102. Gnanasambandam, R., Bae, C., Gottlieb, P.A., and Sachs, F. (2015). Ionic selectivity and permeation properties of human PIEZO1 channels. *PLOS ONE* 10, e0125503.
103. Marchesano, V., Hernandez, Y., Salvenmoser, W., Ambrosone, A., Tino, A., Hobmayer, B., M de la Fuente, J., and Tortiglione, C. (2013). Imaging inward and outward trafficking of gold nanoparticles in whole animals. *ACS Nano* 7, 2431–2442.
104. Böttger, A., Doxey, A.C., Hess, M.W., Pfaller, K., Salvenmoser, W., Deutzmann, R., Geissner, A., Pauly, B., Altstätter, J., Münder, S., *et al.* (2012). Horizontal gene transfer contributed to the evolution of extracellular surface structures: The freshwater polyp Hydra is covered by a complex fibrous cuticle containing glycosaminoglycans and proteins of the PPOD and SWT (Sweet Tooth) families. *PLOS ONE* 7, e52278.
105. Fraune, S., Anton-Erxleben, F., Augustin, R., Franzenburg, S., Knop, M., Schröder, K., Willoweit-Ohl, D., and Bosch, T.C. (2015). Bacteria–bacteria interactions within the microbiota of the ancestral metazoan Hydra contribute to fungal resistance. *ISME J* 9, 1543–1556.

106. Lentz, T.L. (1964). The cell biology of Hydra. Yale Medicine Thesis Digital Library, 877.
107. Philipp, I., Aufschnaiter, R., Ozbek, S., Pontasch, S., Jenewein, M., Watanabe, H., Rentzsch, F., Holstein, T.W., and Hobmayer, B. (2009). Wnt/ $\beta$ -Catenin and noncanonical Wnt signaling interact in tissue evagination in the simple eumetazoan Hydra. Proceedings of the National Academy of Sciences *106*, 4290–4295.
108. Campbell, R.D. (1974). Cell movements in Hydra. American Zoologist *14*, 523–535.

## Publishing Agreement

It is the policy of the University to encourage open access and broad distribution of all theses, dissertations, and manuscripts. The Graduate Division will facilitate the distribution of UCSF theses, dissertations, and manuscripts to the UCSF Library for open access and distribution. UCSF will make such theses, dissertations, and manuscripts accessible to the public and will take reasonable steps to preserve these works in perpetuity.

I hereby grant the non-exclusive, perpetual right to The Regents of the University of California to reproduce, publicly display, distribute, preserve, and publish copies of my thesis, dissertation, or manuscript in any form or media, now existing or later derived, including access online for teaching, research, and public service purposes.

DocuSigned by:  
Taylor Daniel Skokan  
03E9231E50C7467... Author Signature

2/2/2022  
Date